

# Oil & Natural Gas Technology

DOE Award No.: DE-FC26-06NT43067

## Fracture Initiation and Propagation (Task 4 Technical Report)

# Mechanisms Leading to Co-Existence of Gas and Hydrate in Ocean Sediments

Submitted by:

The University of Texas at Austin  
1 University Station C0300  
Austin, TX 78712-0228

Prepared for:

United States Department of Energy  
National Energy Technology Laboratory

May 31, 2008



Office of Fossil Energy

# Mechanisms Leading to Co-existence of Gas and Hydrate in Ocean Sediments

## Task 4: Fracture Initiation and Propagation

for

U.S. Department of Energy  
National Energy Technology Laboratory  
DOE Award DE-FC26-06NT43067

by

**Ruben Juanes**

Department of Civil and Environmental Engineering  
Massachusetts Institute of Technology  
77 Massachusetts Avenue, Room 48-319  
Cambridge, MA 02139  
Phone: 617-253-7191, Fax: 617-258-8850  
Email: [juanes@mit.edu](mailto:juanes@mit.edu)

**Steven L. Bryant**

Department of Petroleum and Geosystems Engineering  
The University of Texas at Austin  
One University Station, Mail Stop C0300  
Austin, TX 78712  
Phone: 512-471-3250, Fax: 512-4719605  
Email: [Steven.Bryant@mail.utexas.edu](mailto:Steven.Bryant@mail.utexas.edu)

May 31, 2008

# TABLE OF CONTENTS

Table of Contents . . . . .	i
List of Tables . . . . .	ii
List of Figures . . . . .	iv
List of Acronyms . . . . .	v
List of Symbols . . . . .	vi
<b>1 INTRODUCTION</b>	<b>1</b>
1.1 Hydrates in natural systems . . . . .	1
1.2 Summary of recent results . . . . .	2
1.3 Scope and organization of this report . . . . .	2
<b>2 THEORY, FORMULATION AND METHODS</b>	<b>4</b>
2.1 Micromechanics of “dry” media . . . . .	4
2.1.1 Micromechanical vs. macroscopic parameters. . . . .	5
2.1.2 Time step selection for mechanics simulation. . . . .	5
2.2 Micro-poromechanics of single-fluid systems . . . . .	6
2.2.1 Biot’s theory of poroelasticity . . . . .	9
2.2.2 Time step selection for fluid flow simulation. . . . .	9
2.3 Micro-poromechanics of two-fluid systems . . . . .	9
<b>3 RESULTS</b>	<b>13</b>
3.1 Micromechanics of “dry” media . . . . .	13
3.1.1 Sediment model generation and initialization . . . . .	13
3.1.2 Uniaxial compaction for “dry” media . . . . .	13
3.1.3 Microscopic vs. macroscopic mechanical parameters . . . . .	13
3.2 Micro-poromechanics of single-fluid systems . . . . .	17
3.2.1 Uniaxial fluid flow . . . . .	17
3.2.2 Uniaxial undrained compaction . . . . .	21
3.3 Micro-poromechanics of two-fluid systems . . . . .	21
3.3.1 Capturing the fracturing phenomenon. . . . .	22
3.3.2 Influence of Earth stresses. . . . .	22
3.3.3 Fracturing vs. capillary invasion: influence of grain size. . . . .	24
<b>4 DISCUSSION AND CONCLUSIONS</b>	<b>27</b>
<b>A FORMULATION DETAILS</b>	<b>28</b>
A.1 Throat conductance . . . . .	28
A.2 Capillary entry pressure . . . . .	30
<b>REFERENCES</b>	<b>34</b>

## List of Tables

1	Macroscopic mechanical parameters for dry samples subject to biaxial compaction. The contact bond strength (in force units) is proportional to the grain size. The resulting elastic and strength parameters are fairly independent of grain size. . . . .	17
2	Macroscopic hydraulic and poromechanical parameters for different grain size distributions. . . . .	20

# List of Figures

1	Forces at a grain–grain contact and the DEM contact model. . . . .	5
2	Conceptual picture of the fluid-solid interaction model at the pore scale when a single fluid is present. . . . .	6
3	Representation of the grain assembly (yellow circles) and the network (green lines). At the center of each fluid domain is a pore body (blue dots). . . . .	7
4	Schematic representation of a fluid domain. At any given time, each fluid domain is characterized by its pore volume $V_p$ , and the pressure $p$ and density $\rho$ of the fluid. Fluid can go in and out of the pore domain at a rate $q_j$ into the neighboring fluid domains. . . . .	8
5	Two modes of methane gas invasion: capillary pressure and fracture opening.	10
6	Meniscus pinning in the presence of two fluid phases in the sediment. . . . .	11
7	Snapshots of the particle settling process. . . . .	14
8	Evolution of the time step during the settling process. . . . .	15
9	Scaling of the time step with grain radius. . . . .	15
10	Experimental stress–strain curves for sediments from Hydrate Ridge [Tan et al., 2006], and comparison with DEM simulations for two different values of the grain stiffness. . . . .	16
11	Inflow and outflow rates into the pressure cell. Comparison of DEM simulation (dotted line) and analytical solution (solid line). . . . .	19
12	Evolution of pressure profiles during the uniaxial fluid flow test. Comparison of DEM simulation (dotted line) and analytical solution (solid line) at different dimensionless times: $\tau = 0.000242, 0.00671, 0.0275, 0.0829, 0.175, 1.404$ . . . . .	20
13	Stress–strain curves for uniaxial undrained compaction. Left: cemented/cohesive sample. Right: unconsolidated/cohesionless sample. . . . .	22
14	Illustration of the fracturing behavior of a model sediment upon injection of gas, when the vertical and horizontal stresses are equal. The sediment fractures “isotropically” into a set of radial, geometrically-complex fractures. . . . .	23
15	Snapshots of the evolution of the methane gas–water interface for the case $r_{\min} = 1$ mm. The pores occupied by gas are represented with blue dots. The brown lines indicate compression at grain–grain contacts. Left: $P_c \approx 0.17$ kPa. Right: $P_c \approx 0.20$ kPa. . . . .	25
16	Snapshots of the evolution of the methane gas–water interface for the case $r_{\min} = 1$ $\mu$ m. The pores occupied by gas are represented with blue dots. The brown lines indicate compression at grain–grain contacts. The green lines represent tension, which is supported by cohesion between grains. Left: $P_c \approx 150$ kPa. Right: $P_c \approx 160$ kPa. . . . .	26
17	Representation of a pore throat in a three-dimensional grain-scale model. The throat is the section with minimum cross-sectional area between two pore bodies. This area is positive even when the surrounding grains are in contact, or even if they overlap. . . . .	29
18	Schematic representation of our conductance model for two-dimensional assemblies. A physically-based throat cross section is defined by assuming cubic packing in the third dimension. . . . .	30

19	Summary of the throat conductance formulation for 2D grain assemblies. . .	31
20	Geometry of the pore throat in the third dimension of a 2D grain-scale model, for the definition of the throat radius . . . . .	33

## List of Acronyms

BSR	Bottom Simulating Reflector
DEM	Discrete Element Method
HSZ	Hydrate Stability Zone
IODP	Integrated Ocean Drilling Program
LSM	Level Set Method
ODP	Ocean Drilling Program
PFC	Particle Flow Code (commercial trademark)

## List of Symbols

$A_j$	effective area of pore throat $j$ [m <sup>2</sup> ]
$b$	Biot coefficient [-]
$c_v$	coefficient of consolidation [Pa]
$C_j$	conductance of pore throat $j$ [m <sup>4</sup> /Pa/s]
$\tilde{C}_j$	dimensionless conductance of pore throat $j$ [-]
$d$	gap at grain–grain “contact” [m]
$\mathbf{F}$	force vector [N]
$F^n$	normal contact force [N]
$F^s$	tangential contact force [N]
$k$	intrinsic permeability [m <sup>2</sup> ]
$k_n$	normal contact stiffness [N/m]
$k_s$	shear contact stiffness [N/m]
$K_f$	bulk modulus of the fluid [Pa]
$K_s$	bulk modulus of the solid grain [Pa]
$L_j$	effective length of pore throat $j$ [m]
$\mathbf{M}$	moment vector [N.m]
$\mathbf{I}_i$	tensor of moments of inertia of grain $i$ [N.m]
$m_i$	mass of particle $i$ [kg]
$p$	fluid pressure [Pa]
$p_D$	dimensionless fluid pressure [-]
$p_g$	gas pressure [Pa]
$p_w$	water pressure [Pa]
$P_c$	capillary pressure [Pa]
$Q_D$	dimensionless fluid flow rate [-]
$q_j$	fluid flow rate through pore throat $j$ [m <sup>3</sup> /s]
$r_g$	grain radius [m]
$r_{\min}$	minimum grain radius of assembly [m]
$\delta t$	time step [s]
$U_n$	grain overlap [m]
$\Delta U_s$	tangential displacement [m]
$V_p$	volume of a pore [m <sup>3</sup> ]
$w(= 1)$	width of 2D assembly in third dimension [m]
$\mathbf{x}_i$	position vector of grain $i$ centroid [m]

### *Greek letters*

$\gamma$	interfacial tension [N/m]
$\boldsymbol{\theta}_i$	angle vector of rotation of grain $i$ [-]
$\mu$	fluid viscosity [Pa.s]
$\bar{\mu}$	contact friction coefficient [-]
$\xi$	dimensionless distance [-]
$\rho_s$	grain density [kg/m <sup>3</sup> ]
$\sigma$	total stress [Pa]
$\sigma'$	effective stress [Pa]

$\sigma_H$	horizontal Earth stress [Pa]
$\sigma_V$	vertical Earth stress [Pa]
$\bar{\sigma}_c$	normal contact strength in stress units [Pa]
$\bar{\tau}_c$	shear contact strength in stress units [Pa]
$\tau$	dimensionless time [-]
$\varphi_n$	normal contact strength in force units [N]
$\varphi_s$	shear contact strength in force units [N]

# 1 INTRODUCTION

## 1.1 Hydrates in natural systems

Methane hydrates are crystalline ice-like compounds, composed of methane molecules caged in a lattice of water molecules [Sloan, 1998]. Hydrates form naturally at high pressures and low temperatures, like those typical of most of the ocean floor. It is believed that an enormous pool of carbon exists in the form of methane gas and methane hydrate in the ocean floor along the continental margins. Some estimates of the size of this reservoir suggest that the amount of energy is of the order of all other fossil fuels combined, although these estimates are highly uncertain [Sloan, 2003]. It also seems likely that this pool of carbon plays an important role in the global carbon cycle [Dickens, 2003], and in massive submarine landslides [Paull et al., 2003].

Methane hydrate systems in ocean sediments have been the subject of intense research in recent years. A significant component of that effort is directed towards gaining a better conceptual picture of the hydrogeological environment of gas hydrate systems. Particular attention has been devoted to the two end-members [Trehu et al., 2006]:

1. The hydrogeologically more active, dynamic end-member, exemplified by Hydrate Ridge, offshore Oregon [Suess et al., 1999; Tryon et al., 2002; Trehu et al., 2004b; Weinberger et al., 2005; Heeschen et al., 2003].
2. The hydrogeologically less active, quiescent end-member, illustrated by Blake Ridge, offshore South Carolina [Holbrook et al., 1996; Dickens et al., 1997].

One of the fundamental observations at these two sites is the co-existence of methane hydrate, gas and brine within the HSZ. This is especially noticeable in dynamic environments [Milkov et al., 2004; Torres et al., 2004], but has been observed in low-flux hydrate provinces [Gorman et al., 2002]. There is by now conclusive evidence that methane transport through the HSZ cannot occur solely as dissolved methane in the aqueous phase. The scientific community is now undergoing a heated debate as to what are the reasons for co-existence [Milkov and Xu, 2005; Torres et al., 2005; Ruppel et al., 2005], which include: (1) kinetics of hydrate formation; (2) regional geotherms; (3) hypersaline brines as a result of hydrate formation; and (4) fast, focused flow of free gas through fractures and high-permeability conduits. The importance of methane migration as a separate gas phase, and the need to account for multiphase flow effects coupled with hydrate formation, have already been pointed out a decade ago [Ginsburg and Soloviev, 1997; Soloviev and Ginsburg, 1997].

It has been proposed that free gas accumulation beneath the HSZ may reach a critical thickness to open fractures in the sediment or activate pre-existing faults that will serve as conduits for fast upwards gas migration [Flemings et al., 2003; Trehu et al., 2004a; Hornbach et al., 2004; Liu and Flemmings, 2006; Weinberger and Brown, 2006]. In this case, it is clear that the study of the hydrate system must be coupled with the mechanical response of the host sediments containing hydrate.

## 1.2 Summary of recent results

Our research is aimed at testing the following hypothesis [Juanes and Bryant, 2006; Behseresht et al., 2008b]: the coupling between drainage and fracturing, both induced by pore pressure, determines whether methane gas entering the hydrate stability zone (HSZ) is converted completely to hydrate. In Behseresht et al. [2008a], a novel implementation of the level set method (LSM) is used to determine the capillarity-controlled displacement of brine by gas from sediment and from fractures within the sediment.

In Jain and Juanes [2008], we present a discrete element method (DEM) to model the strong coupling that takes place between the pore fluids and the mechanical behavior of the sediment. We account rigorously for the presence of one or more fluids in the pore space by incorporating additional sets of forces due to pore fluid pressures and interfacial tension between the fluids. We demonstrate the ability of DEM to reproduce core-scale behavior, as measured by triaxial laboratory experiments and fluid flow tests. The proposed methodology elucidates the depositional environments (grain size, earth stresses, and sediment cohesion) under which migration of methane gas by fracturing of the sediment is favored over capillary invasion. This determines the distribution of methane gas and hydrate which, in turn, has direct implications on the likelihood that gas and hydrate will co-exist, and on the overall size of the energy resource.

## 1.3 Scope and organization of this report

This report presents the formulations and findings under Task 4: *Fracture initiation and propagation* of the DOE/NETL project: *Mechanisms leading to co-existence of gas and hydrate in ocean sediments*. In the original proposal, this task was organized into three subtasks, as follows:

Subtask 4.1: Initialize the model

Subtask 4.2: Hydraulic fracturing with a single-fluid system

Subtask 4.3: Hydraulic fracturing with an elastic membrane representation of a two fluid system

Initialization of a sediment model involves settling, rearrangement and compaction of solid grains. The formulation and verification of the model for each stage is explained in detail in this report. Since the model involves a “dry” medium—one in which the pore fluid is assumed to be infinitely compressible—we propose to rename Subtask 4.1 as: *Micromechanics of “dry” media*.

We have found that single-fluid systems are, under the quasi-static conditions typical of marine hydrogeological environments, not prone to the formation of fractures. This was anticipated in the original proposal and, therefore, we propose to rename Subtask 4.2 as: *Micro-poromechanics of single-fluid systems*.

One of the important research accomplishments has been our ability to model the transition from capillary invasion to fluid fracturing for two-phase systems. Moreover, we have been able to relax the initial assumption of an “elastic membrane” model, and develop a model that incorporates—even if in a simplified fashion—the effect of adhesive forces due to

surface tension. As a result, we propose to rename Subtask 4.3 as: *Micro-poromechanics of two-fluid systems*.

This report is organized in two main sections: (1) Theory, formulation and methods; and (2) Results. Each section is divided into three subsections, corresponding to the three subtasks mentioned above. We discuss our findings—and their relevance—in an integrated fashion in a final section. Some of the technical details of the formulation are given in the appendix.

## 2 THEORY, FORMULATION AND METHODS

The Discrete Element Method (DEM) [Cundall and Strack, 1979] has proved a valuable tool to study the mechanisms for deformation and failure of granular materials with variable degree of cementation [Bruno and Nelson, 1991]. Moreover, based on simple geometric arguments, stress variations (and subsequent deformation) have been shown to affect flow properties such as porosity and permeability [Bruno, 1994].

Each element or grain is identified separately by its own mass, moment of inertia and contact properties. For each grain, its translational and rotational movements are described by solving Newton’s second law of motion. The mechanical behavior at the deformation region of grain contact is approximated by introducing a grain contact model, such as a system of a spring, dashpot and slider (Figure 1).

### 2.1 Micromechanics of “dry” media

The movement of a grain is dictated by the net force and moment acting on it. For a *dry model*, that is, one in which pore pressures are negligible, the forces for each grain may include: (1) contact force  $\mathbf{F}_c$  due to the deformation at the grain contacts, (2) damping forces  $\mathbf{F}_d$  due to grain non-elastic collisions; (3) external forces  $\mathbf{F}_b$  due to gravity and prescribed tractions at the boundaries. The contact force  $\mathbf{F}_c$  can be further split into normal and tangential components,  $\mathbf{F}_c^n$  and  $\mathbf{F}_c^s$ , respectively.

The simplest (linear elastic) mechanical behavior at the grain contacts is described by the following equations:

$$F^n = k_n U_n, \quad \Delta F^s = -k_s \Delta U_s, \quad (1)$$

where  $U_n$  is the overlap,  $\Delta U_s$  is the tangential displacement, and  $k_n$  and  $k_s$  are the normal and shear stiffness at the contact, respectively [ITASCA, 2004; Potyondy and Cundall, 2004]. Inelastic behavior emerges due to either slip between grains, or breakage of contact bonds. Inelasticity is reflected by the constraints:

$$F^s \leq \bar{\mu} F^n, \quad F^n \leq \varphi_n, \quad F^s \leq \varphi_s, \quad (2)$$

where  $\bar{\mu}$  is the contact friction coefficient, and  $\varphi_n$  and  $\varphi_s$  are the normal and shear strengths (in force units) of the contact.

Bulk behavior of a granular system is determined by all individual grain–grain interactions. For the analysis of dry samples, the interactions between particles can be associated with a network of grain–grain contact forces that connects the centroids of grains that are in contact.

Given the set of forces  $\mathbf{F}_j$  and moments  $\mathbf{M}_j$  acting on the  $i$ th particle, its motion is described by the following equations:

$$m_i \ddot{\mathbf{x}}_i = \sum_j \mathbf{F}_j, \quad (3)$$

$$\mathbf{l}_i \ddot{\boldsymbol{\theta}}_i = \sum_j \mathbf{M}_j. \quad (4)$$

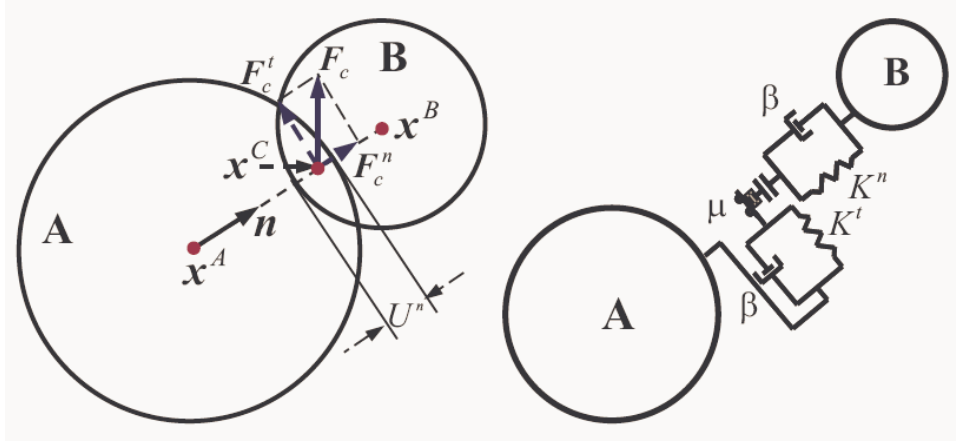


Figure 1: Schematic diagram of a grain–grain contact (left) and the associated contact model in a Discrete Element Model (right) [Jin, 2006].

Here,  $\mathbf{x}_i$  and  $\boldsymbol{\theta}_i$  are the position vector of the grain centroid and the angle vector of rotation about the centroid; the double dots denote second time derivatives of the position and rotation angle;  $m_i$  is the mass; and  $\mathbf{I}_i$  is the tensor of moments of inertia, respectively. The equations of motion (3)–(4) must be solved simultaneously for all grains in the system via a numerical integration scheme. In DEM, explicit solution schemes with a single force evaluation per time step are preferred. A commercial three-dimensional DEM code, PFC2D [ITASCA, 2004], was used.

### 2.1.1 Micromechanical vs. macroscopic parameters.

The parameters that need to be defined at the grain-scale level are  $\rho_s$ ,  $\bar{\mu}$ ,  $k_n$ ,  $k_s$ ,  $\varphi_n$  and  $\varphi_s$ , as well as the grain size distribution, which we shall characterize simply by the radius interval  $[r_{\min}, r_{\max}]$ .

From DEM simulations of biaxial tests, the linear elastic *macroscopic* parameters (Young modulus  $E$  and Poisson ratio  $\nu$ ), as well as strength properties (yield stress  $\sigma_y$ , friction angle  $\varphi$ , cohesion  $c$ , etc.) may be computed. In order to obtain macroscopic parameters that are independent (or only slightly dependent) on the grain size, the contact strengths must scale with the grain size [Potyondy and Cundall, 2004]:

$$\varphi_n = \bar{\sigma}_c 2r_g w, \quad \varphi_s = \bar{\tau}_c 2r_g w, \quad (5)$$

where  $\bar{\sigma}_c$  and  $\bar{\tau}_c$  are the normal and shear contact strengths (in stress units)—assumed to be independent of grain size—and  $w$  is the width of the 2D assembly in the third dimension.

### 2.1.2 Time step selection for mechanics simulation.

Since explicit time integration is used, the time step is bounded by stability considerations. The characteristic time required to capture the dynamics is [ITASCA, 2004]

$$\delta t \sim \sqrt{m_i/k_i}. \quad (6)$$

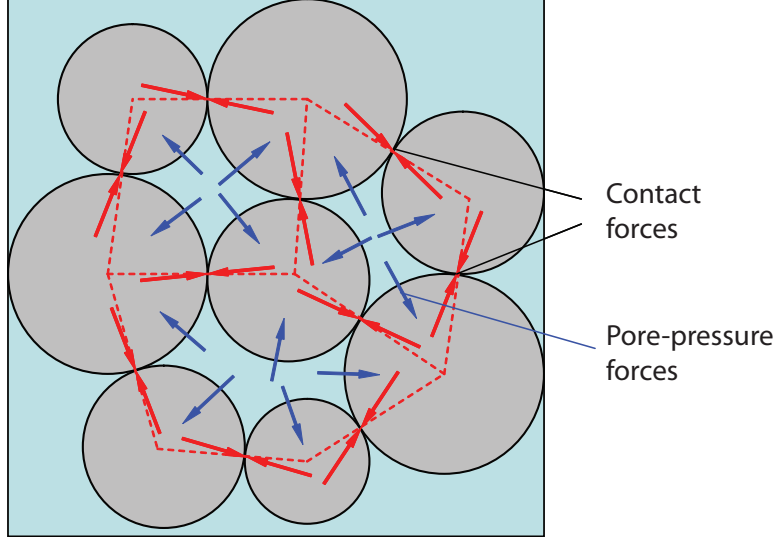


Figure 2: Conceptual picture of the fluid-solid interaction model at the pore scale when a single fluid is present.

In PFC2D, grains are assumed to be disks of unit width ( $w = 1$  m), so  $m = 2\pi r_g^2 w \rho_s$  and, therefore, the critical time step for mechanical stability scales as follows:

$$\delta t_{\text{crit}}^m \sim \sqrt{\rho_s / k_n} r_g, \quad (7)$$

where  $\rho_s$  is the grain density,  $k_n$  is the grain normal stiffness, and  $r_g$  is the grain radius.

## 2.2 Micro-poromechanics of single-fluid systems

From the theory of poromechanics [Biot, 1941], it is well known that pore pressure will influence mechanical behavior. Essentially, compressive stresses in granular media are transmitted both through a solid skeleton and the pore fluids. Recently, models have been developed to incorporate this effect in DEM with a single-phase pore fluid [Shimizu, 2004; Cook et al., 2004; Li and Holt, 2001, 2004].

When the pore space is filled with a single fluid phase at non-negligible pressure, the associated forces must be incorporated in the model. A conceptual view of the new set of forces is shown in Figure 2. Computationally, the model then consists of two overlapping and interacting networks: the grain network and the fluid network. A particular instance is shown in Figure 3. The force that the fluid in one of the domains exerts on a particular grain is obtained by integrating the pressure along the contact area. In our implementation, a pressure force is directed from the midpoint of the segment joining grain contacts to the grain center. Therefore, pressure forces do not induce rotation.

Consider one particular fluid domain, as sketched in Figure 4. The micromechanical equations can be summarized as follows. The flow rate out of the fluid domain through a pore throat is

$$q_j = C_j \frac{p - p_j}{L_j}, \quad (8)$$

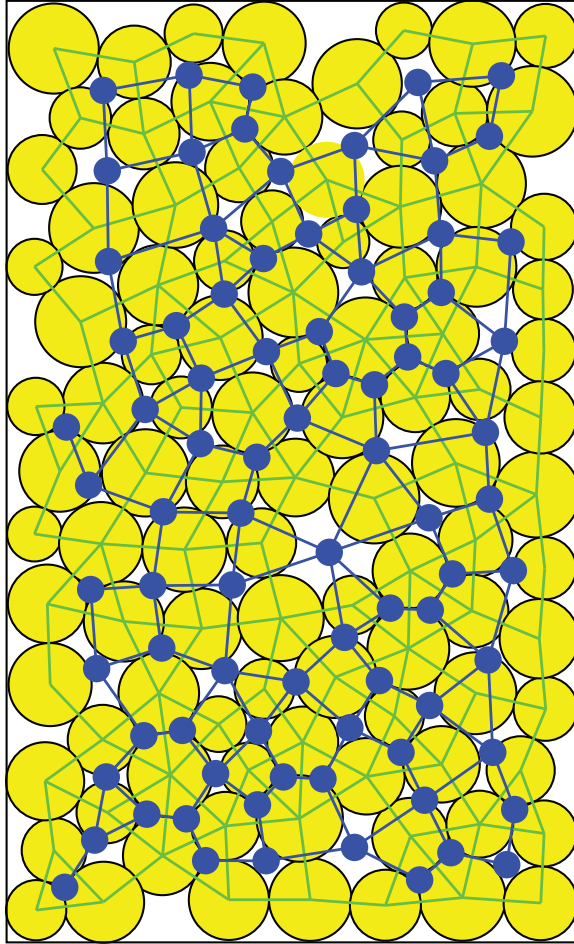


Figure 3: Representation of the grain assembly (yellow circles) and the network (green lines). At the center of each fluid domain is a pore body (blue dots).

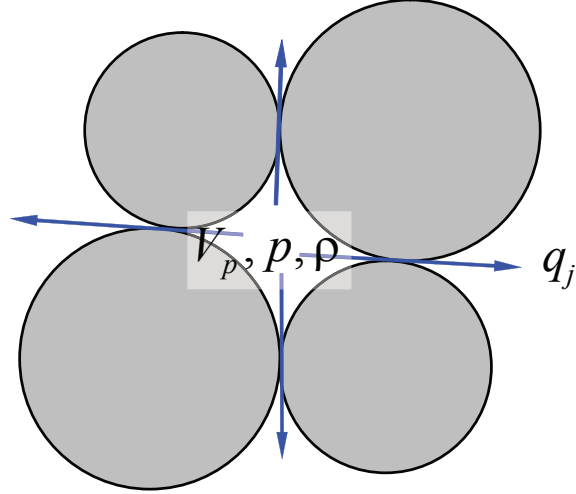


Figure 4: Schematic representation of a fluid domain. At any given time, each fluid domain is characterized by its pore volume  $V_p$ , and the pressure  $p$  and density  $\rho$  of the fluid. Fluid can go in and out of the pore domain at a rate  $q_j$  into the neighboring fluid domains.

where  $C_j$  is the throat conductance and  $L_j$  is an effective distance between pore centers. The conductance is inversely proportional to the fluid viscosity  $\mu$ , and proportional to the square of the effective throat area  $A_j$ :

$$C_j = \frac{\tilde{C}_j}{\mu} \frac{A_j^2}{2r_g} w, \quad (9)$$

where  $\tilde{C}_j$  is a dimensionless throat conductance. The derivation of this equation from the solution of a Stokes flow problem, and the expressions for  $\tilde{C}$  and  $A$ , are given in Appendix A.1.

The grains have certain compressibility, and the radius of a spherical grain varies according to

$$r_g = r_{g,0} \left( 1 - \frac{p}{3K_s} \right), \quad (10)$$

where  $r_{g,0}$  is the initial radius (at zero fluid pressure),  $K_s$  is the bulk modulus of the solid grain, and  $p$  is the average of the pressure around the grain. Finally, mass balance over a fluid domain gives the following pressure evolution equation for a pore volume:

$$\delta p = \frac{K_f}{V_p} \left( -\delta V_p - \sum_j q_j \delta t \right), \quad (11)$$

where  $K_f$  is the fluid bulk modulus, and  $\delta p$  is the pressure variation after a time step  $\delta t$ . The main feature of our model is the term  $-\delta V_p$ , which accounts for the change in volume of each pore caused by changes in grain locations. This term has been neglected in previous investigations of pore-scale poromechanical models but is essential, for example, to reproduce pressurization of the fluid upon fast compaction. It also reflects the reverse coupling present in Biot's self-consistent theory of poroelasticity.

### 2.2.1 Biot’s theory of poroelasticity

There is a formal analogy between the micro-poromechanical equations presented above, and Biot’s self-consistent theory of poroelasticity [Biot, 1941; Wang, 2000]. We expect that the DEM formulation will reproduce the linear theory of poroelasticity only in the range of small deformations and small pressure changes. Under such conditions, the poroelastic parameters can then be determined from DEM simulations. When these conditions are not met, nonlinear/irreversible behavior is expected to emerge in the DEM model, driven by contact slip, bond breaking and grain rearrangement.

### 2.2.2 Time step selection for fluid flow simulation.

The grain-scale fluid flow equations (11) are solved using an explicit time integration scheme. The time step must be restricted for the scheme to be stable. The characteristic time associated with the microscopic fluid flow dynamics is

$$\delta t \sim \frac{V_p}{K_f} \frac{\delta p}{\sum_j q_j}. \quad (12)$$

Introducing Equations (8) and (9), we express the characteristic time as

$$\delta t \sim \frac{V_p}{K_f} \frac{2r_g \mu}{w} \sum_j \frac{L_j}{\tilde{C}_j A_j^2}. \quad (13)$$

Using the scaling  $V_p \sim r_g^2 w$ , and  $A \sim r_g^2$ , the critical time step for fluid flow stability scales as follows:

$$\delta t_{\text{crit}}^f \sim \frac{\mu}{\tilde{C} K_f}. \quad (14)$$

In a coupled poromechanics simulation, the time step must be smaller than the minimum of the critical values in Equations (7) and (14).

## 2.3 Micro-poromechanics of two-fluid systems

In the environments of interest for methane hydrates—in particular, at the base of the hydrate stability zone—two fluid phases exist: a liquid brine phase, and methane gas. One of the key differences between single-fluid and two-fluid systems is the presence of a fluid–fluid interface. Due to surface tension effects, the pressures on both sides of the interface (that is, the pressure of brine and the pressure of methane gas) can be very different.

The key question is: what is the preferential mode of gas invasion? Two different fundamental mechanisms are at play (Figure 5): (1) capillary-dominated invasion of a rigid solid skeleton, and (2) fracturing of the sediment. While capillarity governs invasion of gas through the porous medium, mechanical effects may lead to deformation and fracturing of the sediment skeleton, thereby triggering invasion when it would otherwise not occur. Preferential fracturing of the sediment requires differences in pressure between neighboring pores. While this is typically not a favored scenario in single-fluid systems (unless a fluid is injected at very fast flow rates and pressures, as in hydraulic fracturing operations), it is natural

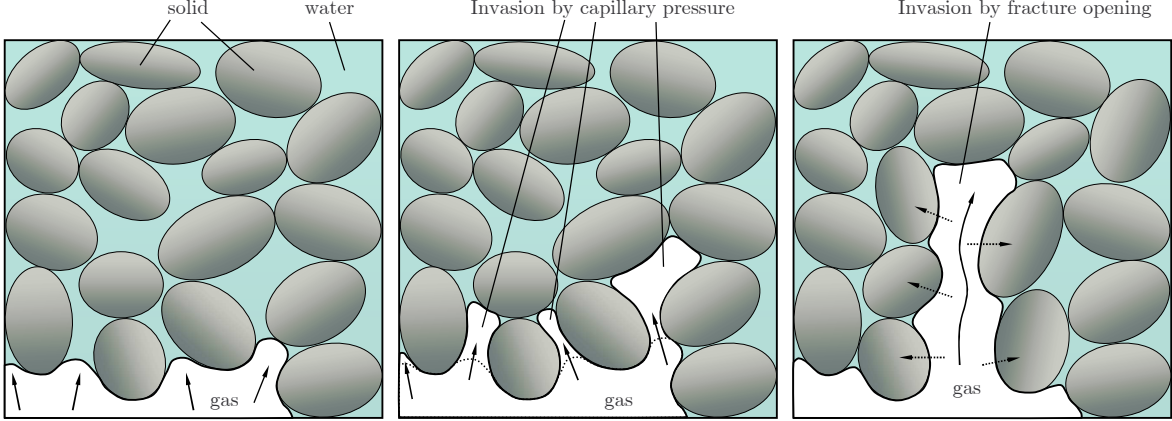


Figure 5: Schematic diagram of the two modes of methane gas invading a sediment. **Top:** before invasion, the gas–water interface of a buoyant gas plume underlies water-filled sediment. **Middle:** invasion will occur if the capillary pressure (the difference between gas pressure and water pressure) exceeds the capillary entry pressure, which is inversely proportional to the pore diameter. **Bottom:** invasion by fracture opening; if the exerted pressure is sufficient to overcome compression and friction at grain contacts, a fracture will form. In a multiphase environment, due to surface tension effects, the gas pressure will *not* dissipate quickly through the porous medium, and water at grain contacts will increase cohesion.

in two-fluid systems because the two fluids have different pressures. Since the two fluids do not mix, a pressure difference does not dissipate. This pressure difference may lead to preferential fracturing of the sediment. Methane invasion by fracture opening is common, as evidenced by field observations of tensile fractures at the seafloor and hydrate layers along bedding planes [Suess et al., 1999]. These processes clearly couple flow and deformation, at both the grain scale and the macroscopic scale.

Here, we adopt an “elastic membrane” representation of the gas/water interface that only allows normal forces to be transmitted (Figure 6). Consider invasion of methane free gas by capillary invasion (Fig. 5(middle)). The gas/water interface will invade a throat if the capillary pressure (that is, the difference between gas pressure and water pressure) is larger than the capillary entry pressure [Richards, 1931; Leverett, 1941; Mayer and Stowe, 1965]. The capillary entry pressure is proportional to the interfacial tension  $\gamma$ , and inversely proportional to the throat opening. Let  $d$  be the throat gap (which, in a 2D model, may be negative if there is overlap between the grains). In Appendix A.2, we derive the following expression for the gas pressure to invade a throat:

$$p_g - p_w \geq \frac{2}{\sqrt{1 + \left(1 + \frac{d}{2r_g}\right)^2} - 1} \frac{\gamma}{r_g}. \quad (15)$$

Clearly, if the grain size is large, this process is favored and gas invasion can occur even if the porous medium is rigid. On the other hand, for small grain size (high capillary entry pressures), gas invasion will not occur until the grains are pushed apart (Fig. 5(bottom)). For cohesionless material, this will occur when the gas pressure exceeds the minimum compressive

Additional cohesion due to surface tension

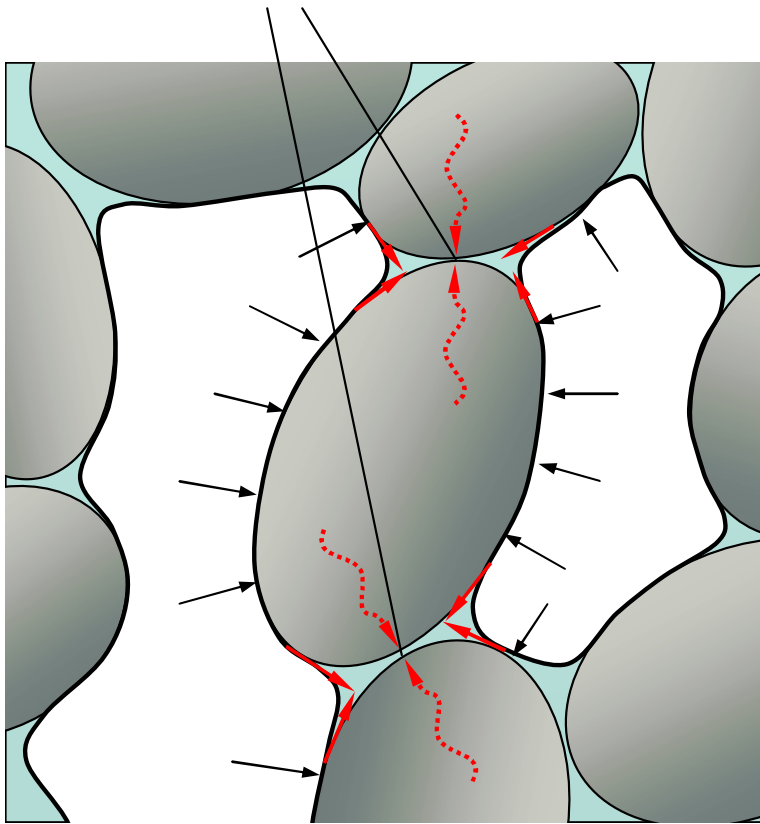


Figure 6: Meniscus pinning in the presence of two fluid phases in the sediment. During multiphase flow in porous media, the least wetting phase (gas) migrates through the center of the pores, while the most wetting phase (brine) coats the grains and forms filaments around the crevices of the pore space. This configuration leads to gas–water menisci around the grain contacts. Due to interfacial tension, these menisci are responsible for an attraction force between grains. At the macroscopic level, this can be interpreted as an increment in the cohesion of the material. This is a purely multiphase-flow effect, not present in single-phase poromechanics.

stress:

$$p_g \geq \sigma_H. \quad (16)$$

This condition of fracture opening must be extended to the case when cohesion  $\bar{\sigma}_c$  exists (either by cementation, consolidation, or capillary adhesion). The fracturing pressure depends not only on the Earth stresses and the cohesive stress, but also on the length of a pre-existing fracture and, importantly, on the grain size. This last dependency emanates from the observation that the internal lengthscale in the fracture toughness is determined by the grain size [Potyondy and Cundall, 2004]. In any case, it is the nonlinear evolution of the DEM micro-poromechanical model that determines when bonds break, and when the gap between grains is large enough for the gas interface to advance, according to Equation (15). In this fashion, the “membrane” advances and a new pore is loaded with a higher pressure.

The implementation of multi-fluid poromechanics is therefore very similar to that of

single-fluid systems, except that the key hydraulic property (the conductance between pore bodies) is set to zero until condition (15) is satisfied.

While capillary invasion and fracture opening are the two end-member mechanisms for methane transport in its own gas phase, our coupled grain-scale model allows us to investigate the competition between the two as a function of grain size, Earth stresses, and sediment cohesion.

## 3 RESULTS

### 3.1 Micromechanics of “dry” media

#### 3.1.1 Sediment model generation and initialization

A model sediment is generated by first choosing the number of particles, and reproducing the desired grain size distribution. As we shall see below, several macroscopic properties (both mechanical and fluid-flow properties) are dependent on the grain size. Therefore, it is important that the sediment model either reproduces the desired grain size distribution, or that the assigned microproperties (e.g. bond strength) reflect the disparity in grain size [Potyondy and Cundall, 2004]. In most of the examples shown in this paper, we have chosen a relatively narrow, uniform distribution  $[r_{\min}, r_{\max}]$ , with  $r_{\max} = (5/3)r_{\min}$ .

The particles are randomly placed in a box and allowed to fall under gravity, simulating sedimentation (Figure 7). The settling process has two differentiating stages: (1) free fall under gravity, with limited grain–grain interaction, and (2) settling and grain rearrangement until static conditions are reached.

In Figure 8 we show the evolution of the time step during the settling process. The time step is larger initially, during the “free fall” stage, and quickly converges to the value required for stability of the dynamical system dominated by grain–grain interactions. The scaling of the time step with grain radius and grain stiffness is shown in Figure 9, confirming the stability condition of Equation (7): the time step is proportional to the grain radius, and inversely proportional to the square root of the grain stiffness.

#### 3.1.2 Uniaxial compaction for “dry” media

Here we show that DEM simulations of “dry” media (infinitely compressible pore fluid) are able to capture the mechanical behavior of real sediments. In Figure 10 we plot experimental stress–strain curves of sediment samples from Hydrate Ridge [Tan et al., 2006] along with curves from DEM simulations. The DEM model sediments reproduce approximately the grain size distribution of actual sediments, and the only parameter that we varied to reproduce measured stress–strain behavior was the grain stiffness  $k_n$ . The rest of the micromechanical parameters are as follows:  $k_s = k_n$ ,  $\bar{\mu} = 0.5$ ,  $\bar{\sigma}_c = \bar{\tau}_c = 0$ .

The DEM simulations match the stress–strain behavior measured in the lab even for very high deformations (up to 25% strain), capturing the material nonlinearity. The DEM model also displays irreversible behavior in that loading/unloading cycles show hysteresis. However, it is unable to reflect the dramatic reduction in stiffness upon unloading that the data show.

#### 3.1.3 Microscopic vs. macroscopic mechanical parameters

One of the potential limitations of DEM models is that, if the model sediment reproduces the grain size distribution of the real sediment, the dimensions of the model are necessarily constrained by the computational requirements. Therefore, it is important to investigate whether the macroscopic behavior of the sediment (small-strain elastic parameters, as well

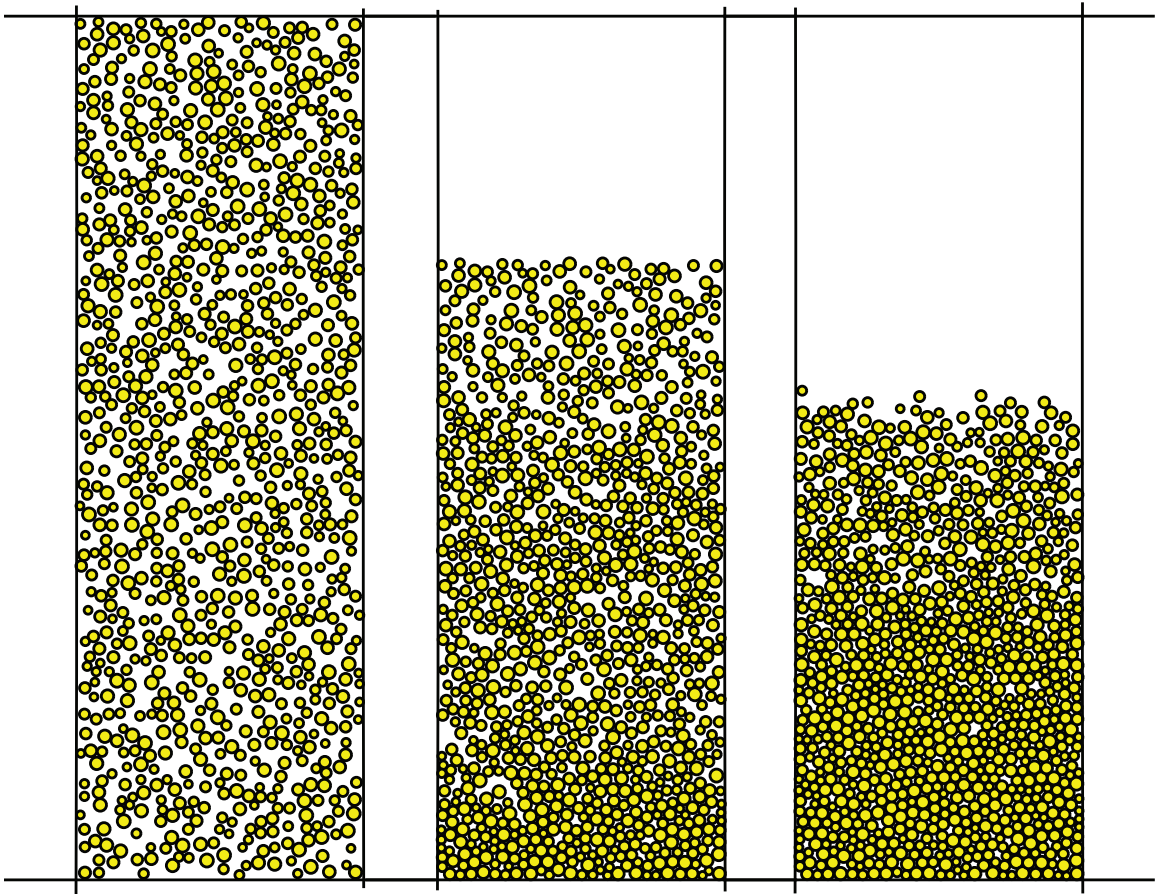


Figure 7: Snapshots of the particle settling process.

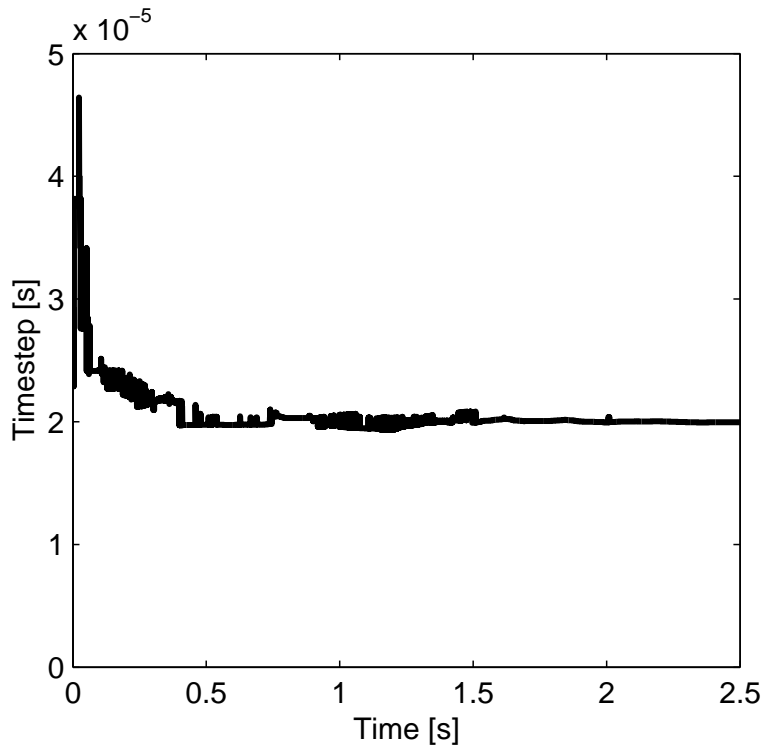


Figure 8: Evolution of the time step during the settling process.

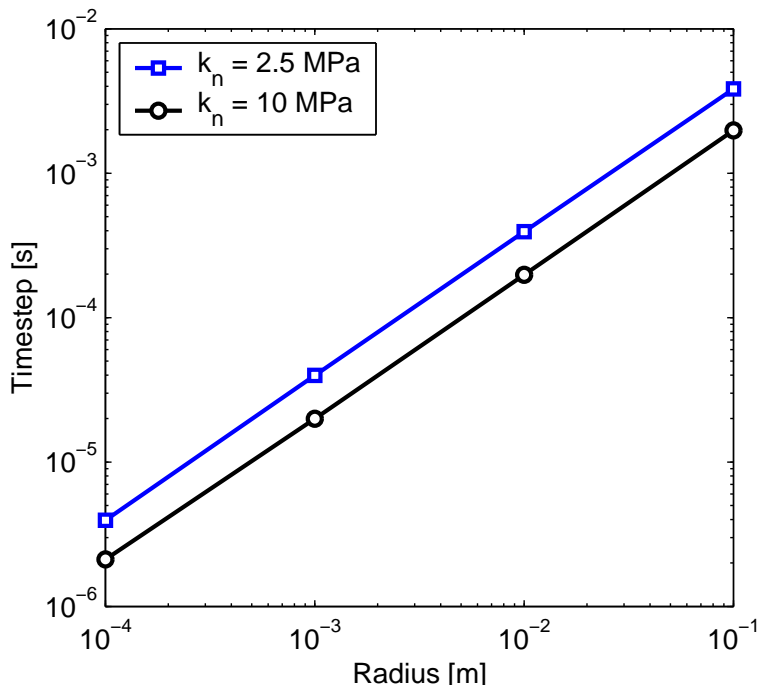


Figure 9: Scaling of the time step with grain radius.

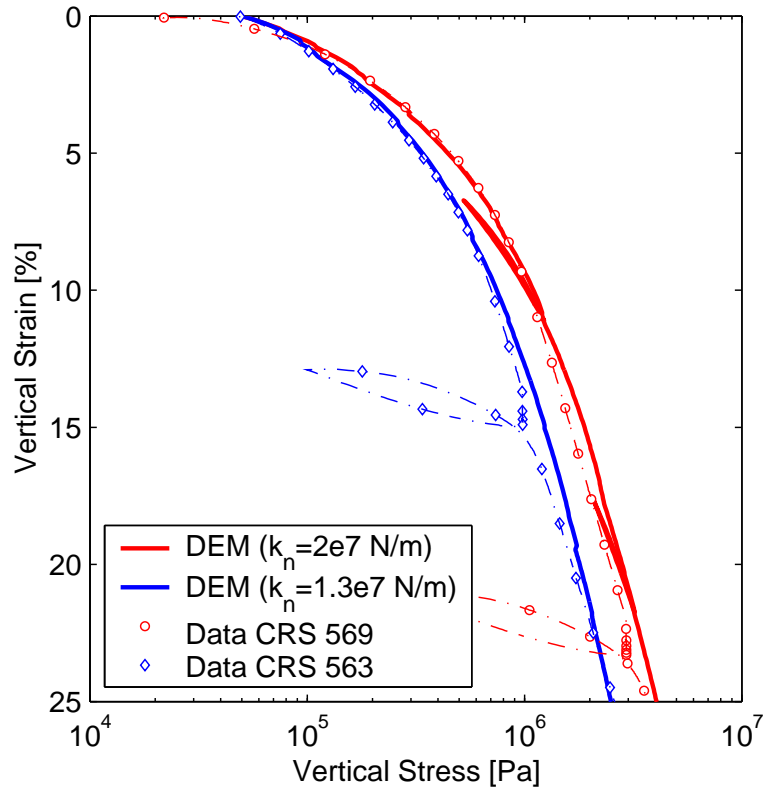


Figure 10: Experimental stress–strain curves for sediments from Hydrate Ridge [Tan et al., 2006], and comparison with DEM simulations for two different values of the grain stiffness.

as strength parameters) can be captured with a different grain size distribution. Here, we confirm that this is indeed the case [Potyondy and Cundall, 2004].

We perform biaxial compression tests on samples with different grain sizes, with  $r_{\min}$  varying from 0.001 m to 0.01 m. All samples are initialized in the same way, therefore leading to virtually the same initial isotropic stress state, with confining stress:  $\sigma_{\text{conf}} = 0.1$  MPa. We fix the following microscopic parameters:  $k_n = 10^7$  N/m,  $k_n/k_s = 2.5$ ,  $\bar{\sigma}_c = \bar{\tau}_c = 0.5$  MPa. The normal and shear contact strengths (in force units) are proportional to the grain size, and given by Equation (5). The lateral walls are smooth, and the confining stress is kept fixed.

For each sample, we record the vertical and horizontal strains,  $\varepsilon_h$  and  $\varepsilon_v$ , as a function of vertical stress  $\sigma_v$ . From these curves, we obtain the peak vertical stress  $\sigma_{v,\text{peak}}$ , and the corresponding vertical and horizontal strains,  $\varepsilon_{v,\text{peak}}$  and  $\varepsilon_{h,\text{peak}}$ . We estimate the “linear” part of the stress–strain curve as the one terminating at 10% of the peak vertical strain. From this linear portion, and assuming plane strain conditions, the Lamé parameters can be determined:

$$\lambda = \frac{\sigma_{\text{conf}} - \frac{\sigma_{v,10} - \sigma_{\text{conf}}}{\varepsilon_{v,10} - \varepsilon_{h,10}}}{\varepsilon_{v,10} + \varepsilon_{h,10}}, \quad G = \frac{1}{2} \frac{\sigma_{v,10} - \sigma_{\text{conf}}}{\varepsilon_{v,10} - \varepsilon_{h,10}}. \quad (17)$$

From these, the Young modulus  $E$  and the Poisson ratio  $\nu$  are readily computed. The results are compiled in Table 1. They confirm that, indeed, the computed macroscopic elastic and strength parameters are fairly independent of the grain size distribution chosen [Potyondy and Cundall, 2004].

Table 1: Macroscopic mechanical parameters for dry samples subject to biaxial compaction. The contact bond strength (in force units) is proportional to the grain size. The resulting elastic and strength parameters are fairly independent of grain size.

$r_{\min}$ [m]	$\sigma_{v,\text{peak}}$ [MPa]	$\varepsilon_{v,\text{peak}}$ [–]	$\varepsilon_{h,\text{peak}}$ [–]	$E$ [MPa]	$\nu$ [–]
0.01	0.472	0.140	0.069	8.43	0.272
0.02	0.510	0.130	0.048	9.08	0.267
0.04	0.481	0.125	0.048	9.34	0.269
0.08	0.539	0.138	0.052	9.22	0.239

## 3.2 Micro-poromechanics of single-fluid systems

### 3.2.1 Uniaxial fluid flow

In this section, we evaluate the fluid flow capabilities of the grain-scale model. We do so by simulating a one-dimensional fluid flow problem in a cell with drained top and bottom boundaries, and impervious fixed lateral boundaries. The initial pressure is constant, and equal to the boundary pressures. Suddenly, a pressure change is applied to the top boundary, and we simulate the evolution of the pressure and fluid inflow/outflow until a new steady state

is reached. The problem is described mathematically by the partial differential equation:

$$c_v \frac{\partial p}{\partial t} - \frac{k}{\mu} \frac{\partial^2 p}{\partial x^2} = 0, \quad 0 < x < H, \quad (18)$$

where  $k$  is the intrinsic permeability,  $\mu$  is the fluid viscosity, and  $c_v$  is the consolidation coefficient [Wang, 2000]. The initial condition is given by:

$$p(x, 0) = 0, \quad 0 \leq x \leq H, \quad (19)$$

and the boundary conditions are:

$$p(0, t) = 0, \quad p(H, t) = \Delta p, \quad t > 0. \quad (20)$$

The problem can be expressed in dimensionless form by defining the following dimensionless quantities:

$$\begin{aligned} \text{distance: } \xi &= \frac{x}{L}, \\ \text{time: } \tau &= \frac{t}{T_c}, \quad T_c = \frac{c_v \mu H^2}{k}, \\ \text{pressure: } p_D &= \frac{p}{\Delta p}, \\ \text{flow rate: } Q_D &= \frac{Q}{Q_c}, \quad Q_c = \frac{k}{\mu} \frac{\Delta p}{H} W w, \end{aligned}$$

where  $W$  is the width and  $w$  is the thickness of the cell (that is, the dimensions of the cell in the directions perpendicular to the flow). The analytical solution to the problem can be found by the method of separation of variables. The dimensionless pressure field is given by:

$$p_D(\xi, \tau) = \xi + \frac{2}{\pi} \sum_{n=1}^{\infty} \frac{(-1)^n}{n} \sin(n\pi\xi) \exp(-(n\pi)^2\tau). \quad (21)$$

By differentiating the expression above, we find the expression for the dimensionless flow rate in and out of the cell:

$$Q_D^{\text{in}} = 1 + 2 \sum_{n=1}^{\infty} (-1)^n \cos(n\pi) \exp(-(n\pi)^2\tau), \quad (22)$$

$$Q_D^{\text{out}} = 1 + 2 \sum_{n=1}^{\infty} (-1)^n \exp(-(n\pi)^2\tau). \quad (23)$$

The objective is to determine whether the grain-scale model reproduces the macroscopic behavior. The relevant macroscopic parameters are the intrinsic permeability  $k$  and the consolidation coefficient  $c_v$ . The intrinsic permeability is obtained by matching the flow rate at steady state. The consolidation coefficient is determined by matching the dimensionless inflow and outflow curves.

We generated an assembly with 1000 grains, and a minimum radius  $r_{\min} = 1$  cm. The vertical and horizontal dimensions of the cell are, approximately,  $H = 1$  m and  $W = 0.7$  m.

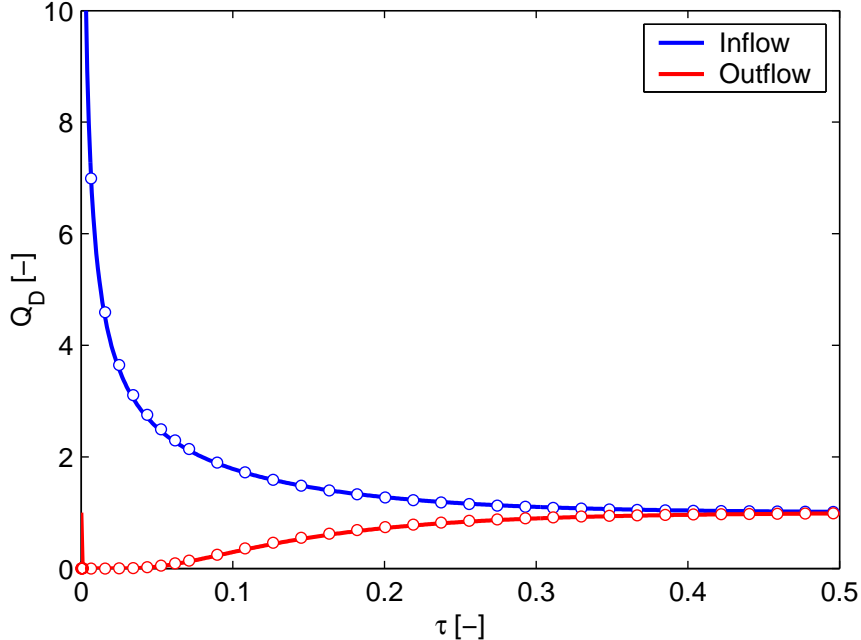


Figure 11: Inflow and outflow rates into the pressure cell. Comparison of DEM simulation (dotted line) and analytical solution (solid line).

We set the pressure increment  $\Delta p$  to a small value, so that the effects of pore pressure on the mechanical deformation are minimal. Once the flow stabilizes, inflow and outflow rates are equal to  $Q_c$ , and the intrinsic permeability of the medium can be computed as:

$$k = \frac{\mu H Q_c}{W w \Delta p}. \quad (24)$$

The characteristic time  $T_c$  is then obtained by matching the numerical inflow and outflow curves, from which the macroscopic consolidation coefficient is computed as:

$$c_v = \frac{k T_c}{\mu H^2}. \quad (25)$$

In Figure 11 we plot the dimensionless inflow and outflow rates as a function of dimensionless time. The agreement between the DEM results and the analytical solution is remarkable, indicating that the flow formulation accurately captures the macroscopic behavior (Darcy flow in porous media). As a further validation of the model, we compare in Figure 12 the evolution of dimensionless pore pressure within the sample. By plotting the pressure values from the DEM simulation at individual pores, we obtain a scattered profile of the average pressure as a function of depth. We compare these results with the analytical solution at different dimensionless times. Again, the agreement is remarkable.

By repeating the fluid flow simulations with different values of  $r_{\min}$ , we determine the dependence of the hydraulic and poromechanical parameters on grain size. The results are compiled in Table 2, where we confirm that the intrinsic permeability scales with the square of the grain size (as expected from Stokes theory, and the Kozeny–Carman relation

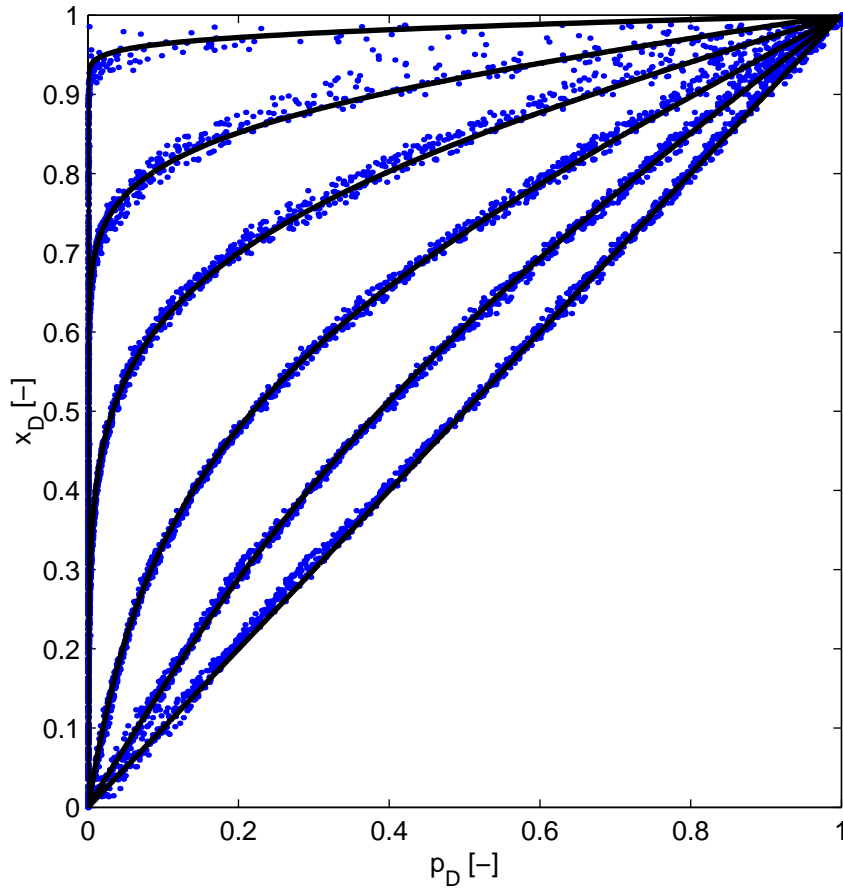


Figure 12: Evolution of pressure profiles during the uniaxial fluid flow test. Comparison of DEM simulation (dotted line) and analytical solution (solid line) at different dimensionless times:  $\tau = 0.000242, 0.00671, 0.0275, 0.0829, 0.175, 1.404$ .

Table 2: Macroscopic hydraulic and poromechanical parameters for different grain size distributions.

$r_{\min}$ [m]	$k$ [m <sup>2</sup> ]	$c_v/K_f$ [-]
0.01	$0.289 \times 10^{-6}$	0.161
0.001	$0.289 \times 10^{-8}$	0.156

for granular materials). Moreover, if the fluid is significantly more compressible than the skeleton, the DEM simulations also reflect that the effective consolidation coefficient  $c_v$  is inversely proportional to  $K_f$ , with the constant of proportionality being approximately equal to the porosity.

### 3.2.2 Uniaxial undrained compaction

A sensitive test towards validation of the DEM coupled model is fluid–solid behavior during undrained consolidation tests. A sediment model is initialized by gravitational settling. Then the walls are adjusted to achieve an isotropic confining stress state of 0.1 MPa. Until that point, the fluid is allowed to drain and the pressure is atmospheric ( $p = 0$  MPa). After that, the sample is sealed so that no fluid is allowed to drain, and it is subjected to uniaxial compaction. During the undrained compaction process, the vertical strain  $\varepsilon$ , total vertical stress  $\sigma$ , and average pore pressure  $p$  are recorded. In view of the effective stress concept [Terzaghi, 1943; Biot, 1941], the total stress required to achieve a given deformation in a fluid-saturated medium is larger than for a dry medium. In the realm of the linear theory of poroelasticity, the *effective stress* is given by:

$$\sigma' = \sigma - bp, \quad (26)$$

where  $b$  is the Biot coefficient. The dependence of the Biot coefficient on the solid and fluid properties of the constituents is reasonably well understood [Coussy, 1995; Wang, 2000]. The Biot coefficient approaches a value of one only in the limit of incompressible grains. If the grain and fluid compressibilities are comparable, the Biot coefficient is less than one.

We used an assembly with 100 grains,  $r_{\min} = 0.01$  m,  $k_n = 10^7$  N/m,  $k_n/k_s = 2.5$ , and  $K_f = 10^7$  Pa. In Figure 13 we show the stress–strain curves for a cemented/cohesive sample (bond strength  $\bar{\sigma}_c = \bar{\tau}_c = 10^6$  Pa—top figure), and for an unconsolidated/cohesionless sample (bond strength  $\bar{\sigma}_c = \bar{\tau}_c = 10^2$  Pa—bottom figure). In both cases, we plot the stress–strain curves for the fluid-saturated medium (total stress), and for a dry medium. We confirm that the dry stress curve can be interpreted as the effective stress, and recovered by subtracting the pore pressure times the Biot coefficient from the total stress. In this way, the Biot coefficient can be inferred. Figure 13 illustrates the proper behavior of the coupled DEM model in two ways: (1) the results are in agreement with the Biot theory of poroelasticity (at least in the region of small strains); and (2) the values of  $b$  inferred from the simulation also agree well with experimental values [Wang, 2000, Table C.1].

## 3.3 Micro-poromechanics of two-fluid systems

Migration of a gas phase through a deformable medium may occur by two end-member mechanisms: (1) capillary invasion through a rigid medium, and (2) fracture opening. Our DEM model is capable of reproducing *both* mechanisms, and therefore predict the conditions under which one is favored over the other, and gas migration as a result of their *combined* effect.

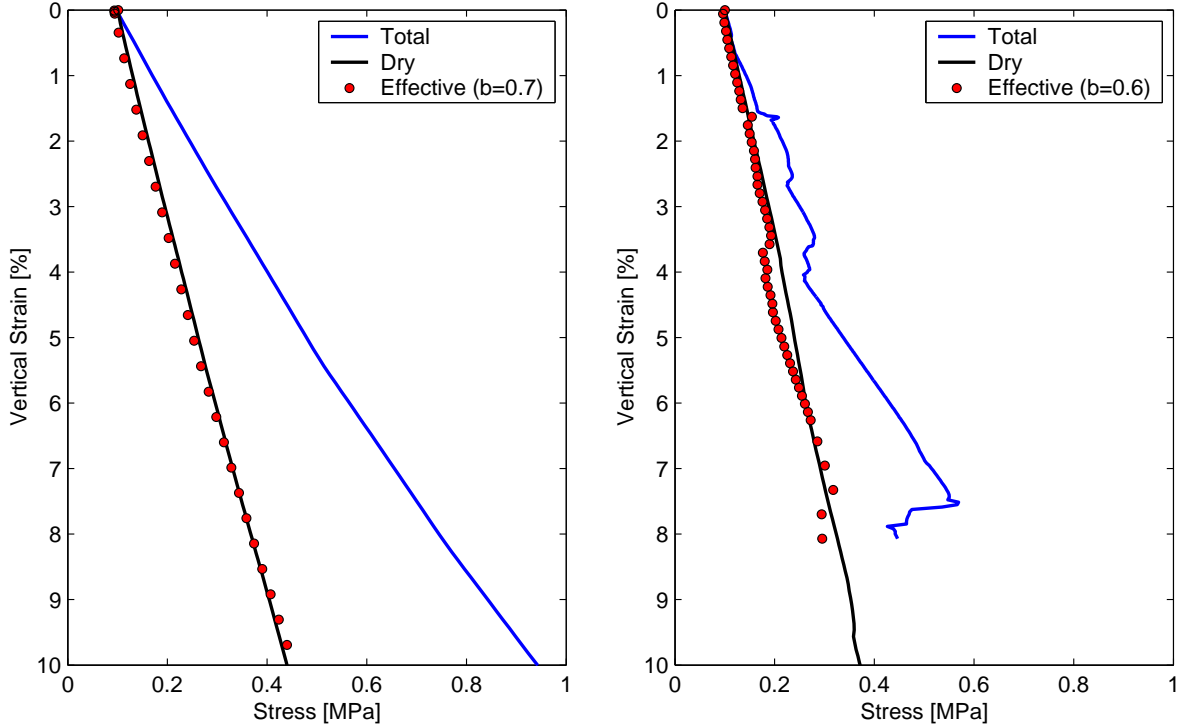


Figure 13: Stress–strain curves for uniaxial undrained compaction. Left: cemented/cohesive sample. Right: unconsolidated/cohesionless sample.

### 3.3.1 Capturing the fracturing phenomenon.

We first illustrate that our DEM model of coupled two-phase fluid flow and grain mechanics can reproduce fracture initiation and propagation, upon invasion of an immiscible gas phase. As explained earlier, we adopt an “elastic membrane” representation of the gas/water interface that only allows normal forces to be transmitted. The formulation of adhesion forces due to surface tension effects [Orr et al., 1975] is greatly simplified at this stage. If the gas cannot invade a throat by capillarity, the gas pressure will act to separate the grains. When the bond between two grains is lost, and the gap between them increases sufficiently, the “membrane” advances and a new pore is loaded with a higher pressure.

### 3.3.2 Influence of Earth stresses.

In many (passive) depositional environments, the horizontal stress is lower than the vertical stress. In such scenarios, one expects the development of vertical fractures that open up the sediment in the direction of minimum compressive stress.

In Figure 14 we show that fracturing of the sediment is not necessarily restricted to anisotropic Earth stresses. Even when horizontal and vertical stresses are equal, the medium tends to fracture in a set of radial, geometrically complex fractures, if gas is injected into a brine-saturated sediment.

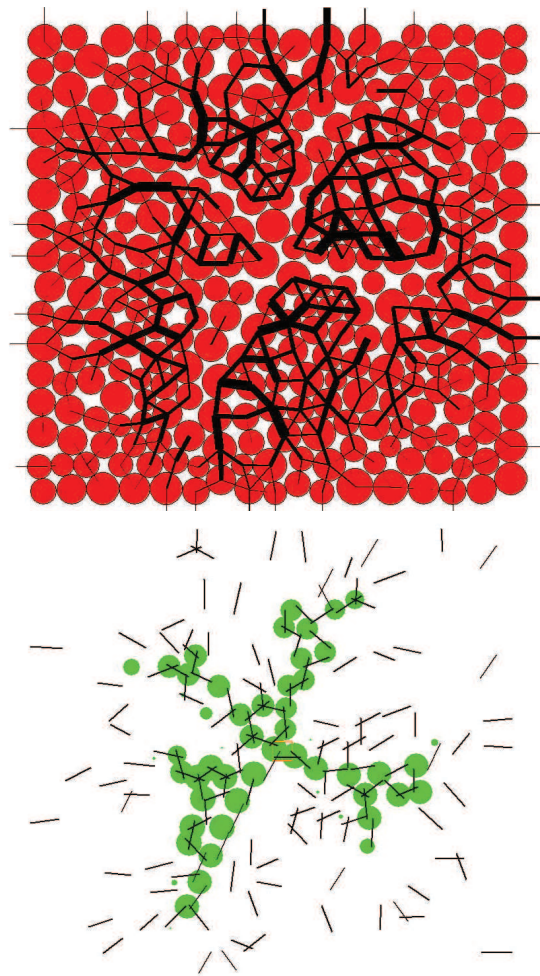


Figure 14: Illustration of the fracturing behavior of a model sediment upon injection of gas, when the vertical and horizontal stresses are equal. The sediment fractures “isotropically” into a set of radial, geometrically-complex fractures.

### 3.3.3 Fracturing vs. capillary invasion: influence of grain size.

We find that the most sensitive factor in determining the mode of methane gas transport (sediment fracturing or capillary invasion) is the grain size: fracturing is favored for fine-grained sediments, while capillary invasion is favored for coarse-grained sediments. We will report on our theoretical analysis of this competition, as well as on the quantitative validation of the coupled grain-scale model, in future communications. Here we simply illustrate the two end-member systems.

The simulation is set up as follows. A sample of 300 grains of grain size  $[r_{\min}, 2r_{\min}]$  is generated by gravitational settling. The sediment is compacted under constant pore pressure until a desired stress state is achieved. We impose an anisotropic stress state, with effective stresses  $\sigma'_v = 10$  kPa, and  $\sigma'_h \approx 8$  kPa. The interfacial tension is  $\gamma = 50 \times 10^{-3}$  N/m. We assume that the cohesion is inversely proportional to grain radius. This is phenomenologically adequate (fine-grained material like clays are cohesive) and is also consistent with the adhesive forces that result from the presence of a gas–water interface [Kato et al., 2004]. For simplicity, we take  $\bar{\sigma}_c = 10\gamma/r_g$ . The only parameter that is left free is the grain size  $r_{\min}$ .

In Figure 15 we show two snapshots of the evolution of the methane–water interface for a coarse-grain sediment of characteristic size  $r_{\min} = 1$  mm. It is apparent that during the invasion of methane gas, there is virtually no movement of the solid grains: the sediment acts like a rigid skeleton. Indeed, the network of grain contact compressive forces remains the same during the process. Invasion of gas from pore to pore occurs when the gas pressure (minus the water pressure) exceeds the capillary entry pressure of the throat (Equation (15)). In this case, the capillary entry pressure is much lower than the fracturing pressure (the left figure corresponds to  $P_c \approx 0.17$  kPa), and fluid transport is well described by *invasion percolation* [Wilkinson and Willemsen, 1983; Lenormand et al., 1988]. Ultimately, if the gas pressure is sufficiently high, almost all the pores have been invaded by methane gas. In this case, this occurs at a slightly higher capillary entry pressure of  $P_c \approx 0.2$  kPa.

The behavior is completely different when a much smaller grain size is used. The evolution of the methane gas migration for  $r_{\min} = 1$   $\mu\text{m}$  is shown in Figure 16. The range of capillary entry pressure for the initial configuration is now in the order of 150 kPa. However, at this pressure, mechanical effects are become dominant, and the solid skeleton no longer behaves like a rigid medium. At around  $P_c \approx 150$  kPa, the invading gas starts to initiate a fracture, with its characteristic stress concentration at the fracture tip captured by the DEM model [Potyondy and Cundall, 2004] (left plot). At a slightly higher pressure ( $P_c \approx 160$  kPa), the fracture propagates vertically. The case presented here is interesting in that it displays *some* competition between fracture opening and capillary invasion—note the invaded pores to the right of the fracture. Fracture opening, however, dominates the vertical migration of methane in its free gas form.

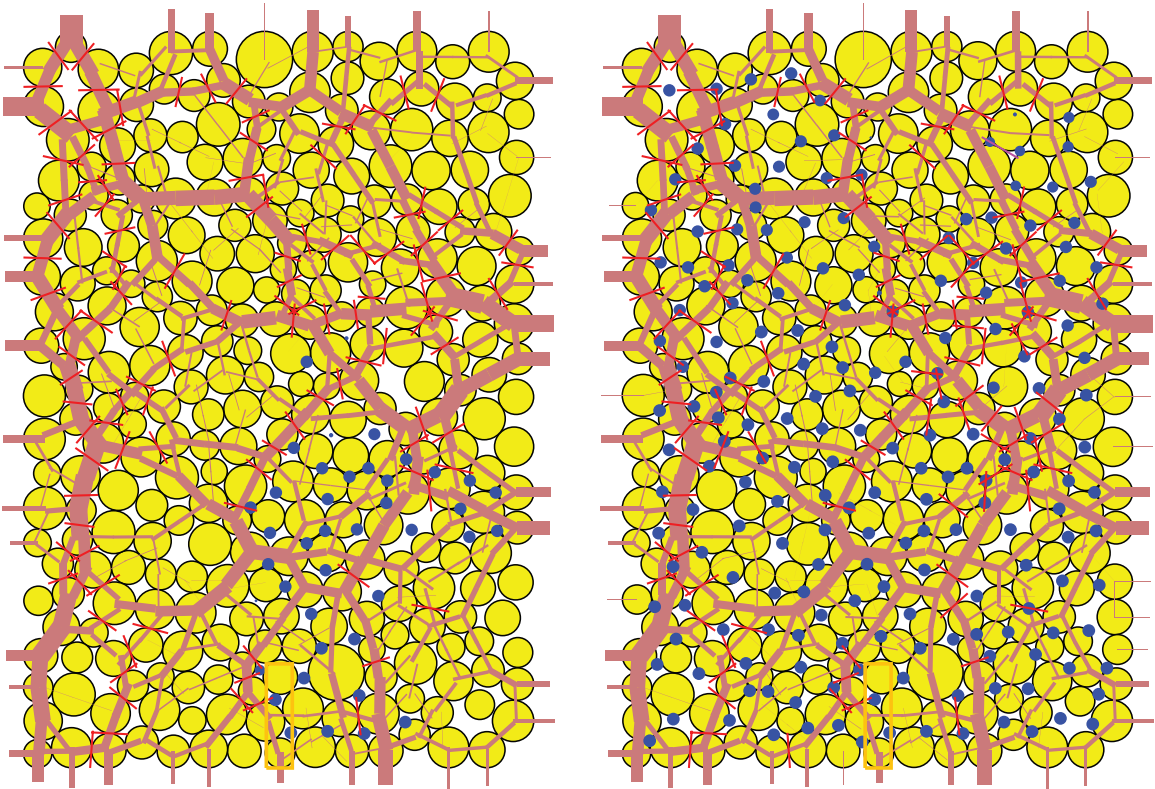


Figure 15: Snapshots of the evolution of the methane gas–water interface for the case  $r_{\min} = 1$  mm. The pores occupied by gas are represented with blue dots. The brown lines indicate compression at grain–grain contacts. Left:  $P_c \approx 0.17$  kPa. Right:  $P_c \approx 0.20$  kPa.

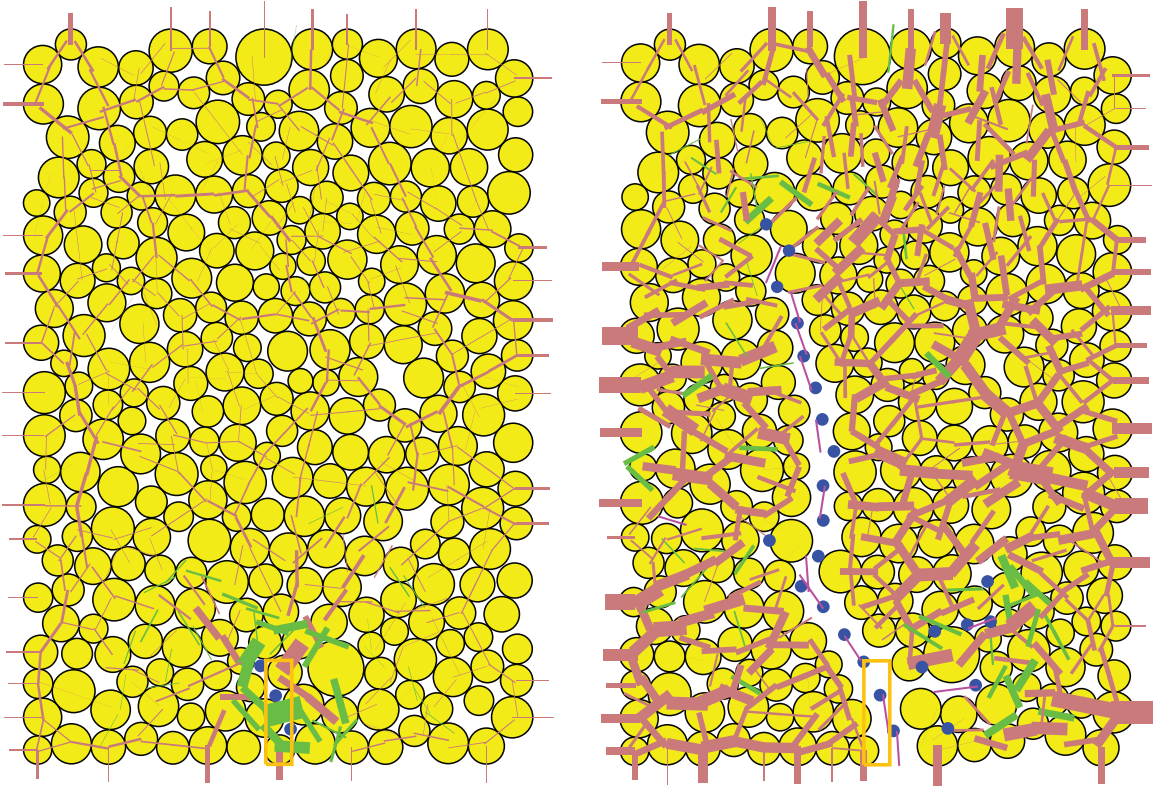


Figure 16: Snapshots of the evolution of the methane gas–water interface for the case  $r_{\min} = 1 \mu\text{m}$ . The pores occupied by gas are represented with blue dots. The brown lines indicate compression at grain–grain contacts. The green lines represent tension, which is supported by cohesion between grains. Left:  $P_c \approx 150 \text{ kPa}$ . Right:  $P_c \approx 160 \text{ kPa}$ .

## 4 DISCUSSION AND CONCLUSIONS

We have presented a discrete element model for the simulation, at the grain scale, of gas migration in brine-saturated deformable media. The model has been validated for many processes, including: (1) generation of sediment models by gravitational settling and compaction; (2) stress–strain behavior of ocean sediments; (3) transient single-phase flow for determination of hydraulic parameters; (4) undrained compaction tests for determination of poromechanical parameters.

The coupled model permits investigating an essential process that takes place at the base of the hydrate stability zone: the upward migration of methane in its own free gas phase. We elucidate the way in which gas migration may take place: (1) by capillary invasion in a rigid-like medium; and (2) by initiation and propagation of a fracture.

Each end member can be analyzed separately, and conditions for gas invasion can be found the capillary-dominated and fracture-dominated regimes. The significant contribution of our coupled model is that it captures both phenomena and, as a result, allows us to study the transition between the two regimes.

We find that the main factor controlling the mode of gas transport in the sediment is the grain size. We have shown that coarse-grain sediments favor capillary invasion, whereas fracturing dominates in fine-grain media.

These emergent phenomena have important implications for understanding hydrates in natural systems (either ocean sediments and permafrost regions). Our model predicts that, in fine sediments, hydrate will likely form in veins that follow a fracture-network pattern. Since the mechanism of fracture propagation is self-reinforcing, our results indicate that it is possible, and even likely, that methane gas will penetrate deeply into the HSZ (and maybe all the way to the ground surface). The hydrate concentration in this type of accumulations will likely be quite low.

Our model supports the view that, in coarse sediments, the buoyant methane gas is likely to invade the pore space more uniformly, in a process akin to invasion percolation. While this is definitely affected by heterogeneity in grain-size distribution, the overall pore occupancy is likely to be much higher than for a fracture-dominated regime.

The predictions from our model are entirely consistent with field observations of hydrates in natural systems [Suess et al., 1999; Flemings et al., 2003; Trehu et al., 2004a; Hornbach et al., 2004; Liu and Flemmings, 2006; Weinberger and Brown, 2006].

# A FORMULATION DETAILS

## A.1 Throat conductance

In this section we derive Equation (9) for the throat conductance. Our formulation resolves one fundamental problem of two-dimensional grain-scale models: the fact that when grains are in contact, the aperture of the throat between pores is zero. Three-dimensional models do not suffer from this problem, because the throat can be associated with the section of minimum cross-sectional area between two pore bodies.

Before discussing our formulation for 2D models, consider an individual pore throat in 3D, as shown in Figure 17. A throat can be assimilated to a microfluidics pipe, with a certain angular cross section. For creeping flow in a small channel, the Navier-Stokes equations reduce to the elliptic Poisson equation. For a coordinate system in which one of the axes (say, the  $z$ -axis) is parallel to the channel, the equation and boundary conditions describing the flow read [Bird et al., 1960]:

$$\nabla^2 v = -\frac{\Xi}{\mu} \quad \text{in } \Omega, \quad (27)$$

$$\Xi = -\frac{\partial p}{\partial z}, \quad (28)$$

$$v(x, y) = 0 \quad \text{on } \partial\Omega, \quad (29)$$

where  $\mu$  is the fluid viscosity,  $\Xi$  is the (negative) pressure gradient, and  $\partial\Omega$  is the boundary of the two-dimensional cross section  $\Omega$ .

Many solutions exist to this equation exist for simplified geometries, and useful parameterizations have been developed in the context of pore-network models of fluid-flow through rocks [Øren et al., 1998; Patzek and Silin, 2001]. The total flowrate  $q$  through the throat cross section can be expressed in the following form:

$$q \equiv \int_{\Omega} v(x, y) \, d\Omega = C\Xi, \quad (30)$$

where  $C$  is the throat conductance. Dimensional analysis dictates that the conductance can, in turn, be expressed as follows:

$$C = \frac{1}{\mu} A^2 \tilde{C}, \quad (31)$$

where  $A$  is the cross-sectional area of the throat, and  $\tilde{C}$  is a dimensionless conductance. It has been shown that, for a very wide range of throat shapes, the dimensionless conductance is simply a function of the shape factor,

$$G = \frac{A}{P^2}, \quad (32)$$

where  $P$  is the perimeter of the throat. In fact, for triangular cross sections, the dimensionless conductance can be approximated by the simple expression [Patzek and Silin, 2001]:

$$\tilde{C} = \frac{3}{5}G. \quad (33)$$

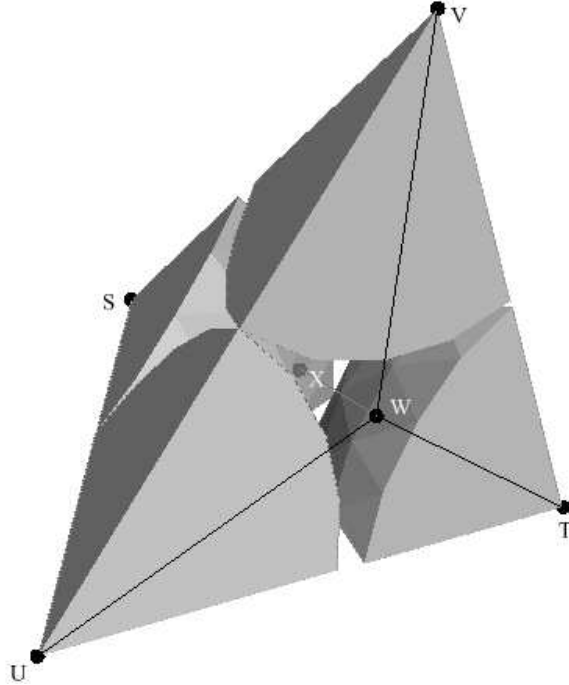


Figure 17: Representation of a pore throat in a three-dimensional grain-scale model. The throat is the section with minimum cross-sectional area between two pore bodies. This area is positive even when the surrounding grains are in contact, or even if they overlap.

With precise knowledge of the geometry of the grain assembly, one could compute the area and shape factor for each throat, and evaluate the throat conductance using the expressions above. However, since these equations themselves rely on the assumption of creeping flow in cylindrical channels, it is sufficient to consider a “master” geometry (like the one shown in Figure 17). In any case, it is important to note that the throat conductance scales with the fourth power of the grain size:

$$C \sim \frac{\tilde{C}}{\mu} r_g^4. \quad (34)$$

The question is: how do we apply this conductance formulation to two-dimensional grain-scale models? In 2D models, the cross section (or aperture) of a pore throat is zero if grains are in contact. This would lead to a model through that does not conduct fluid. To address this issue, previous investigations typically resort to defining an artificial throat aperture using heuristic arguments [Bruno and Nelson, 1991; Li and Holt, 2001, 2004; ITASCA, 2004].

We resolve this problem by understanding a two-dimensional model as a vertical cross section of a three-dimensional model. We must make some approximations with respect to the grain arrangement in the third dimension. In particular, we assume cubic packing of the 3D assembly. Consider two grains of the same size that are in contact in the 2D model (Figure 18). For cubic packing in the third dimension, the geometry of the throats is well defined, and the flow rate through an individual throat can be computed with Equations (30)–(31).

Importantly, this model leads to physically-realistic throat geometries (and, therefore, throat conductances) regardless of whether the two grains defining a throat are just in

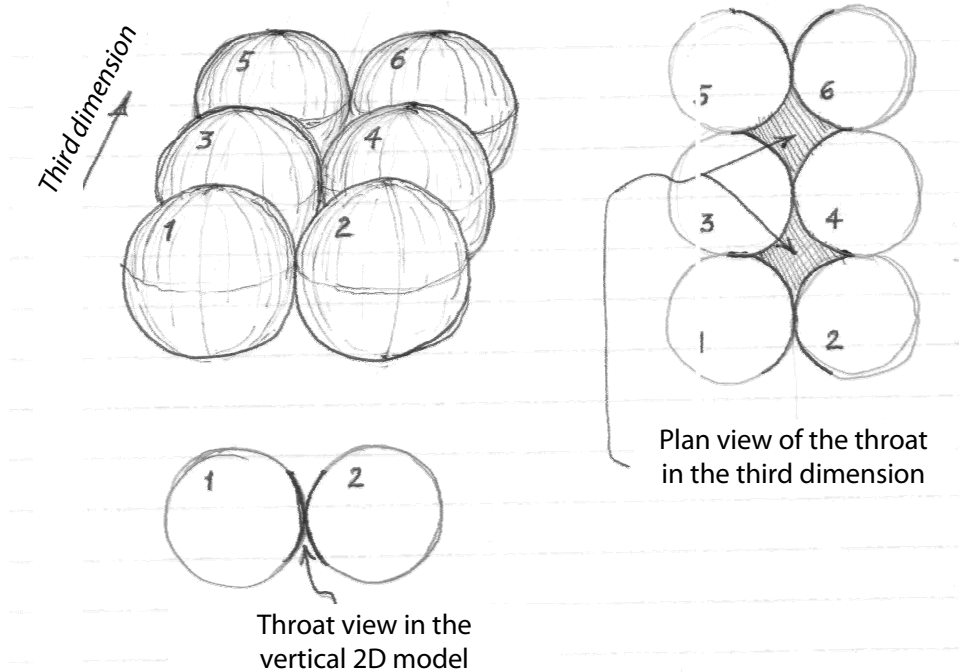


Figure 18: Schematic representation of our conductance model for two-dimensional assemblies. A physically-based throat cross section is defined by assuming cubic packing in the third dimension.

contact (gap  $d = 0$ ), whether there is a gap between them ( $d > 0$ ), or whether there is overlap between them ( $d < 0$ ). For each configuration, the shape factor can be computed using elementary geometry, and the dimensionless conductance evaluated therefrom. In Figure 19, we summarize the throat conductance formulation for 2D grain assemblies.

In a 2D model, we must collapse the third dimension, and compute the flow rate between pore bodies as

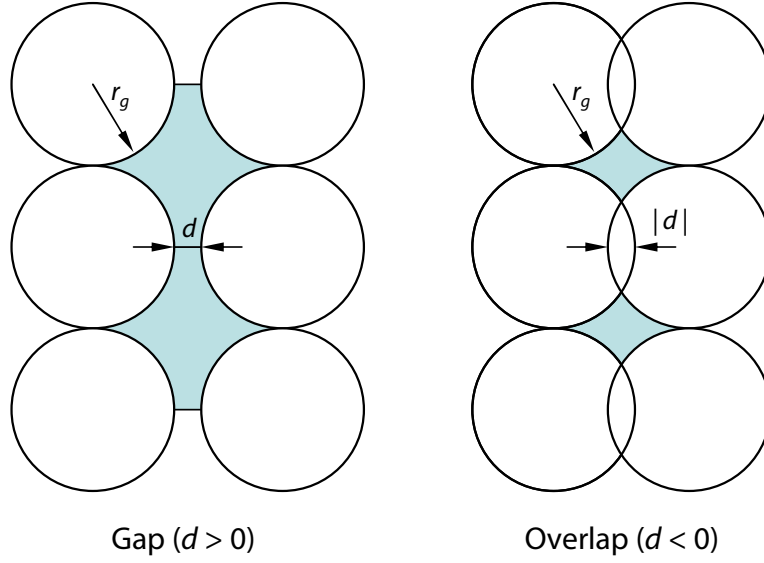
$$q_{2D} = q_{3D} \times N_{\text{th}} = q_{3D} \frac{w}{2r_g}, \quad (35)$$

where, if  $w = 1$ ,  $Q$  is the flowrate per unit width. Combining Equation (35) with (30) and (31) leads to Equation (8) and (9), as desired.

## A.2 Capillary entry pressure

The conceptual model presented above also provides a framework to determine capillary entry pressures in two-dimensional models, which is required to simulate two-phase flow.

Consider, first, invasion of gas through a throat in a three-dimensional setting (Figure 17). The surface tension between gas and brine is  $\gamma$ , and the contact angle between the gas–water interface and the solid surface is  $\theta$ . Gas will penetrate through the throat cross section when the capillary pressure (the gas pressure minus the water pressure) exceeds the threshold capillary pressure. The Mayer–Stowe–Princen (MSP) [Mayer and Stowe, 1965; Princen, 1969a,b, 1970] method for calculating the threshold pressure relies on equation the curvature of the corner arc menisci to the curvature of the invading interface. Expressions




---

If  $d > 0$  (gap)

$$A = 4r_g^2 \left( 1 - \frac{\pi}{4} + \frac{d}{r_g} \right)$$

$$P = 2r_g \left( \pi + \frac{2d}{r_g} \right)$$

Elseif  $d \leq 0$  (overlap)

$$A = 4r_g^2 \left( 1 - \sqrt{\frac{|d|}{r_g} - \left( \frac{|d|}{2r_g} \right)^2} \right) \left( 1 - \frac{|d|}{r_g} \right)$$

$$\alpha = \sin^{-1} \left( 1 - \frac{|d|}{2r_g} \right)$$

$$P = 2r_g \cdot 2\alpha$$

Endif

$$G = \frac{A}{P^2}$$

$$\tilde{C} = \frac{3}{5}G$$


---

Figure 19: Summary of the throat conductance formulation for 2D grain assemblies.

for the drainage capillary entry pressure have been derived for a variety of cross sections [Mason and Morrow, 1991; Øren et al., 1998; Patzek, 2001]. They take the form:

$$P_c^e = \frac{2\gamma}{r_{\text{th}}} F(\theta, G, D), \quad (36)$$

where  $r_{\text{th}}$  is the radius of the inscribed circle, and  $F$  is a function of the receding contact angle and the geometry of the throat—through the throat shape factor  $G$  and a function  $D$  of the throat corner angles. It turns out that, if the contact angle is small (as it normally is for gas invasion into a natural sediment),  $F \approx 1$  [Lenormand et al., 1983; Patzek, 2001]. Therefore, for zero contact angle, the capillary entry pressure can be approximated by

$$P_c^e = \frac{2\gamma}{r_{\text{th}}}. \quad (37)$$

For a throat formed in the space between three spherical grains of equal radius  $r_g$  that are in contact, elementary geometry leads to the expression:

$$r_{\text{th}} = r_g \left( \frac{2}{\sqrt{3}} - 1 \right), \quad (38)$$

and, therefore, we obtain the simple and useful estimate:

$$P_c^e \approx 10 \frac{\gamma}{r_g}. \quad (39)$$

Once again, we apply this concept to two-dimensional grain-scale models, by assuming simple cubic packing in the third dimension. In this way, we can rigorously define a throat radius (and, from it, a capillary entry pressure) even when the 2D throat aperture is zero (because the 2D grains defining a pore throat are in contact). If the two grains are exactly in contact (see Figure 20), one can immediately obtain the relation:

$$r_{\text{th}} = r_g(\sqrt{2} - 1). \quad (40)$$

When the two grains of equal size are separated by a gap ( $d > 0$ ), or when they overlap ( $d < 0$ ), the relation above can be extended as follows:

$$r_{\text{th}} = r_g \left( \sqrt{1 + \left(1 + \frac{d}{2r_g}\right)^2} - 1 \right). \quad (41)$$

Substituting Equation (41) into (37) leads to Equation (15), as desired.

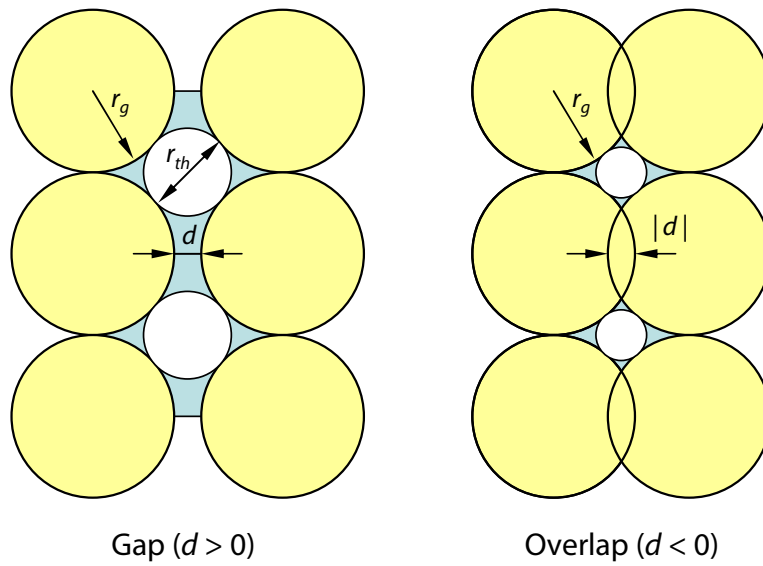


Figure 20: Geometry of the pore throat in the third dimension of a 2D grain-scale model, for the definition of the throat radius

## REFERENCES

- J. Behseresht, Y. Peng, M. Prodanovic, and S. L. Bryant. Pore-scale mechanistic study of the preferential mode of hydrate formation in sediments: Role of capillarity. In *Proc. 6th Intl. Conf. Gas Hydrates (ICGH 2008)*, Vancouver, Canada, July 6–10, 2008a.
- J. Behseresht, Y. Peng, M. Prodanovic, S. L. Bryant, A. K. Jain, and R. Juanes. Mechanisms by which methane gas and methane hydrate coexist in ocean sediments. In *Offshore Technology Conference*, Houston, TX, May 5–8, 2008b. (OTC 19332).
- M. A. Biot. General theory of three-dimensional consolidation. *J. Appl. Phys.*, 12(155–164), 1941.
- R. B. Bird, W. E. Stewart, and E. N. Lightfoot. *Transport Phenomena*. John Wiley and Sons, New York, 1960.
- M. S. Bruno. Micromechanics of stress-induced permeability anisotropy and damage in sedimentary rocks. *Mech. Mater.*, 18:31–48, 1994.
- M. S. Bruno and R. B. Nelson. Microstructural analysis of the inelastic behavior of sedimentary rock. *Mech. Mater.*, 12(2):95–118, 1991.
- B. K. Cook, D. R. Noble, and J. R. Williams. A direct simulation method for particle-fluid systems. *Eng. Comput.*, 21(2–4):151–168, 2004.
- O. Coussy. *Mechanics of Porous Media*. John Wiley & Sons, Chichester, England, 1995. Originally published in French as *Mécanique des Milieux Poreux*, Editions Technip, 1991.
- P. A. Cundall and O. D. L. Strack. Discrete numerical model for granular assemblies. *Geotechnique*, 29:47–65, 1979.
- G. R. Dickens. Rethinking the global carbon cycle with a large, dynamic and microbially mediated gas hydrate capacitor. *Earth Planet. Sci. Lett.*, 213:169–183, 2003.
- G. R. Dickens, C. K. Paull, and P. Wallace. Direct measurement of in situ methane quantities in a large gas-hydrate reservoir. *Nature*, 385:426–428, 1997.
- P. B. Flemings, X. Liu, and W. J. Winters. Critical pressure and multiphase flow in Blake Ridge gas hydrates. *Geology*, 31(12):1057–1060, 2003.
- G. D. Ginsburg and V. A. Soloviev. Methane migration within the submarine gas-hydrate stability zone under deep-water conditions. *Mar. Geol.*, 137:49–57, 1997.
- A. R. Gorman, W. S. Holbrook, M. J. Hornbach, K. L. Hackwith, D. Lizarralde, and I. Pecher. Migration of methane gas through the hydrate stability zone in a low-flux hydrate province. *Geology*, 30(4):327–330, 2002.
- K. U. Heeschen, A. M. Trehu, R. W. Collier, E. Suess, and G. Rehder. Distribution and height of methane bubble plumes on the Cascadia Margin characterized by acoustic imaging. *Geophys. Res. Lett.*, 30(12):Art. No. 1643, doi:10.1029/2003GL016974, 2003.

- W. S. Holbrook, H. Hoskins, W. T. Wood, R. A. Stephen, and D. Lizarralde. Methane hydrate and free gas on the Blake Ridge from vertical seismic profiling. *Science*, 273:1840–1842, September 27, 1996.
- M. J. Hornbach, D. M. Saffer, and W. S. Holbrook. Critically pressured free-gas reservoirs below gas-hydrate provinces. *Nature*, 427(6970):142–144, 2004.
- ITASCA. *PFC2D, v3.1 – Theory and Background*. Itasca Consulting Group, Inc., Minneapolis, MN, 2004.
- A. K. Jain and R. Juanes. Pore-scale mechanistic study of the preferential mode of hydrate formation in sediments: Coupling of multiphase fluid flow and sediment mechanics. In *Proc. 6th Intl. Conf. Gas Hydrates (ICGH 2008)*, Vancouver, Canada, July 6–10, 2008.
- G. Jin. *Physics-Based Modeling of Sedimentary Rock Formation and Prediction of Transport Properties*. PhD Dissertation, University of California at Berkeley, Spring 2006.
- R. Juanes and S. L. Bryant. Mechanisms leading to co-existence of methane gas and hydrate in ocean sediments. Technology status assessment report, U.S. Department of Energy, DOE/NETL Grant DE-FC26-06NT43067, November 2006.
- S. Kato, T. Sakakibara, and H. Yoshimori. Effects of intergranular adhesive force on behavior of granular material. In Y. Shimizu, R. D. Hart, and P. Cundall, editors, *Numerical Modeling in Micromechanics Via Particle Methods. Proc. of the 2nd International PFC Symposium, Kyoto, Japan*, pages 347–354, Balkema, Leiden, October 2004.
- R. Lenormand, E. Touboul, and C. Zarcone. Numerical models and experiments on immiscible displacements in porous media. *J. Fluid Mech.*, 189:165–187, 1988.
- R. Lenormand, C. Zarcone, and A. Sarr. Mechanisms of the displacement of one fluid by another in a network of capillary ducts. *J. Fluid Mech.*, 135:123–132, 1983.
- M. C. Leverett. Capillary behavior of porous solids. *Petrol. Trans. AIME*, 142:152–169, 1941.
- L. Li and R. M. Holt. Simulation of flow in sandstone with fluid coupled particle model. In *Rock Mechanics in the National Interest. Proceedings of the 38th U.S. Rock Mechanics Symposium, Washington, D.C.*, volume 1, pages 165–172, Balkema, Rotterdam, July 2001.
- L. Li and R. M. Holt. A study on the calculation of particle volumetric deformation in a fluid coupled PFC model. In Y. Shimizu, R. D. Hart, and P. Cundall, editors, *Numerical Modeling in Micromechanics Via Particle Methods. Proc. of the 2nd International PFC Symposium, Kyoto, Japan*, pages 273–279, Balkema, Leiden, October 2004.
- X. Liu and P. B. Flemmings. Passing gas through the hydrate stability zone at southern Hydrate Ridge, offshore Oregon. *Earth Planet. Sci. Lett.*, 241:211–216, 2006.
- G. Mason and N. R. Morrow. Capillary behavior of a perfectly wetting liquid in irregular triangular tubes. *J. Colloid Interface Sci.*, 141:262, 1991.

- R. P. Mayer and R. A. Stowe. Mercury-porosimetry breakthrough pressure for penetration between packed spheres. *J. Colloid Interface Sci.*, 20:893, 1965.
- A. V. Milkov, G. R. Dickens, G. E. Claypool, Y.-J. Lee, W. S. Borowski, M. E. Torres, W. Xu, H. Tomaru, A. M. Trehu, and P. Schultheiss. Co-existence of gas hydrate, free gas, and brine within the regional gas hydrate stability zone at Hydrate Ridge (Oregon margin): evidence from prolonged degassing of a pressurized core. *Earth Planet. Sci. Lett.*, 222:829–843, 2004.
- A. V. Milkov and W. Xu. Comment on “Gas hydrate growth, methane transport, and chloride enrichment at the southern summit of Hydrate Ridge, Cascadia margin off Oregon” by Torres et al. [Earth Planet. Sci. Lett. 226:225–241 (2004)]. *Earth Planet. Sci. Lett.*, 239:162–167, 2005.
- P. E. Øren, S. Bakke, and O. J. Arntzen. Extending predictive capabilities to network models. *Soc. Pet. Eng. J.*, 3(4):324–336, December 1998.
- F. M. Orr, L. E. Scriven, and A. P. Rivas. Pendular rings between solids: meniscus properties and capillary force. *J. Fluid Mech.*, 67:723–742, 1975.
- T. W. Patzek. Verification of a complete pore network simulator of drainage and imbibition. *Soc. Pet. Eng. J.*, 6(2):144–156, June 2001.
- T. W. Patzek and D. B. Silin. Shape factor and hydraulic conductance in noncircular capillaries: I. One-phase creeping flow. *J. Colloid Interface Sci.*, 296:295–304, 2001.
- C. K. Paull, P. G. Brewer, W. Ussler, E. T. Peltzer, G. Rehder, and D. Clague. An experiment demonstrating that marine slumping is a mechanism to transfer methane from seafloor gas-hydrate deposits into the upper ocean and atmosphere. *Geo-Mar. Lett.*, 22:198–203, 2003.
- D. O. Potyondy and P. A. Cundall. A bonded-particle model for rock. *Int. J. Rock Mech. Min. Sci.*, 41:1329–1364, 2004.
- H. M. Princen. Capillary phenomena in assemblies of parallel cylinders. I. Capillary rise between two cylinders. *J. Colloid Interface Sci.*, 30:60, 1969a.
- H. M. Princen. Capillary phenomena in assemblies of parallel cylinders. II. Capillary rise in systems with more than two cylinders. *J. Colloid Interface Sci.*, 30:359, 1969b.
- H. M. Princen. Capillary phenomena in assemblies of parallel cylinders. III. Liquid columns between horizontal parallel cylinders. *J. Colloid Interface Sci.*, 34:171, 1970.
- L. A. Richards. Capillary conduction of liquids through porous mediums. *Physics*, 1:318–333, 1931.
- C. Ruppel, G. R. Dickens, D. G. Castellini, W. Gilhooly, and D. Lizarralde. Heat and salt inhibition of gas hydrate formation in the northern Gulf of Mexico. *Geophys. Res. Lett.*, 32:L04605, doi:10.1029/2004GL021909, 2005.

- Y. Shimizu. Fluid coupling in PFC2D and PFC3D. In Y. Shimizu, R. D. Hart, and P. Cundall, editors, *Numerical Modeling in Micromechanics Via Particle Methods. Proc. of the 2nd International PFC Symposium, Kyoto, Japan*, pages 281–287, Balkema, Leiden, October 2004.
- E. D. Sloan. *Clathrate Hydrates of Natural Gases*. Marcel Dekker, New York, second edition, 1998.
- E. D. Sloan. Fundamental principles and applications of natural gas hydrates. *Nature*, 426:353–359, November 23, 2003.
- V. A. Soloviev and G. D. Ginsburg. Water segregation in the course of gas hydrate formation and accumulation in submarine gas-seepage fields. *Mar. Geol.*, 137:59–68, 1997.
- E. Suess, M. E. Torres, G. Bohrmann, R. W. Collier, J. Greiner, P. Linke, G. Rehder, A. Trehu, K. Wallman, G. Winckler, and E. Zuleger. Gas hydrate destabilization: enhanced dewatering, benthic material turnover and large methane plumes at the Cascadia convergent margin. *Earth Planet. Sci. Lett.*, 170:1–15, 1999.
- B. B. Tan et al. Data report: Consolidation and strength characteristics of sediments from ODP Site 1244, Hydrate Ridge, Cascadia continental margin. In *Proc. Ocean Drilling Program, Sci. Results*, volume 204, 2006.
- K. Terzaghi. *Theoretical Soil Mechanics*. John Wiley, New York, 1943.
- M. E. Torres, K. Wallman, A. M. Trehu, G. Bohrmann, W. S. Borowski, and H. Tomaru. Gas hydrate growth, methane transport, and chloride enrichment at the southern summit of Hydrate Ridge, Cascadia margin off Oregon. *Earth Planet. Sci. Lett.*, 226:225–241, 2004.
- M. E. Torres, K. Wallman, A. M. Trehu, G. Bohrmann, W. S. Borowski, and H. Tomaru. Reply to comment on: “Gas hydrate growth, methane transport, and chloride enrichment at the southern summit of Hydrate Ridge, Cascadia margin off Oregon”. *Earth Planet. Sci. Lett.*, 239:168–175, 2005.
- A. M. Trehu, P. B. Flemings, N. L. Bangs, J. Chevalier, E. Gracia, J. E. Johnson, C.-S. Liu, X. Liu, M. Riedel, and M. E. Torres. Feeding methane vents and gas hydrate deposits at south Hydrate Ridge. *Geophys. Res. Lett.*, 31:L23310, doi:10.1029/2004GL021286, 2004a.
- A. M. Trehu, P. E. Long, M. E. Torres, G. Bohrmann, F. R. Rack, T. S. Collett, D. S. Goldberg, A. V. Milkov, M. Riedel, P. Schultheiss, N. L. Bangs, S. R. Barr, W. S. Borowski, G. E. Claypool, M. E. Delwiche, G. R. Dickens, E. Gracia, G. Guerin, M. Holland, J. E. Johnson, Y. J. Lee, C. S. Liu, X. Su, B. Teichert, H. Tomaru, M. Vanneste, M. Watanabe, and J. L. Weinberger. Three-dimensional distribution of gas hydrate beneath southern Hydrate Ridge: constraints from ODP Leg 204. *Earth Planet. Sci. Lett.*, 222:845–862, 2004b.

- A. M. Trehu, C. Ruppel, M. Holland, G. R. Dickens, M. E. Torres, T. S. Collett, D. Goldberg, R. Riedel, and P. Schultheiss. Gas hydrates in marine sediments: lessons from scientific drilling. *Oceanography*, 19(4):124–143, 2006.
- M. D. Tryon, K. M. Brown, and M. E. Torres. Fluid and chemical flux in and out of sediments hosting methane hydrate deposits on Hydrate Ridge, OR, II: Hydrological processes. *Earth Planet. Sci. Lett.*, 201:541–557, 2002.
- H. F. Wang. *Theory of Linear Poroelasticity*. Princeton University Press, 2000.
- J. L. Weinberger and K. M. Brown. Fracture networks and hydrate distribution at Hydrate Ridge, Oregon. *Earth Planet. Sci. Lett.*, 245:123–136, 2006.
- J. L. Weinberger, K. M. Brown, and P. E. Long. Painting a picture of gas hydrate distribution with thermal images. *Geophys. Res. Lett.*, 32:L04609, doi:10.1029/2004GL021437, 2005.
- D. Wilkinson and J. Willemsen. Invasion percolation: a new form of percolation theory. *J. Phys. A*, 16:3365–3376, 1983.

## **National Energy Technology Laboratory**

626 Cochrans Mill Road  
P.O. Box 10940  
Pittsburgh, PA 15236-0940

3610 Collins Ferry Road  
P.O. Box 880  
Morgantown, WV 26507-0880

One West Third Street, Suite 1400  
Tulsa, OK 74103-3519

1450 Queen Avenue SW  
Albany, OR 97321-2198

2175 University Ave. South  
Suite 201  
Fairbanks, AK 99709

Visit the NETL website at:  
[www.netl.doe.gov](http://www.netl.doe.gov)

Customer Service:  
1-800-553-7681

